



**HAL**  
open science

## Numerical assessment of Diffuse-Interface method for air-assisted liquid sheet simulation

Benoît Péden, Julien Carmona, Pierre Boivin, Schmitt Thomas, Bénédicte Cuenot, Nicolas Odier

► **To cite this version:**

Benoît Péden, Julien Carmona, Pierre Boivin, Schmitt Thomas, Bénédicte Cuenot, et al.. Numerical assessment of Diffuse-Interface method for air-assisted liquid sheet simulation. 2024. hal-04383131

**HAL Id: hal-04383131**

**<https://hal.science/hal-04383131>**

Preprint submitted on 9 Jan 2024

**HAL** is a multi-disciplinary open access archive for the deposit and dissemination of scientific research documents, whether they are published or not. The documents may come from teaching and research institutions in France or abroad, or from public or private research centers.

L'archive ouverte pluridisciplinaire **HAL**, est destinée au dépôt et à la diffusion de documents scientifiques de niveau recherche, publiés ou non, émanant des établissements d'enseignement et de recherche français ou étrangers, des laboratoires publics ou privés.

# Numerical assessment of Diffuse-Interface method for air-assisted liquid sheet simulation

Benoît Pédén<sup>a,\*</sup>, Julien Carmona<sup>b,1</sup>, Pierre Boivin<sup>c</sup>, Thomas Schmitt<sup>d</sup>,  
Bénédicte Cuenot<sup>b</sup>, Nicolas Odier<sup>a,b</sup>

<sup>a</sup>*CECI, Université de Toulouse, CERFACS/CNRS, 31100, Toulouse, France*

<sup>b</sup>*CERFACS, 42, Avenue Gaspard Coriolis, 31057 Toulouse, France*

<sup>c</sup>*Aix Marseille Univ, CNRS, Centrale Marseille, M2P2, Marseille, France*

<sup>d</sup>*Laboratoire EM2C, CNRS, CentraleSupélec, Université Paris-Saclay, 3, rue Joliot-Curie, 91192 Gif-sur-Yvette, France*

---

## Abstract

This study presents the implementation and validation of a second-order accurate solver for the 4-equation multi-fluid method in a cell-vertex context, to handle aeronautical air-assisted liquid sheet configurations. Validations include Laplace tests, droplets oscillations, and a two-dimensional configuration reminiscent of an aeronautical airblast injector. Promising results are obtained in the last case, especially when the pressure is increased, as relevant for aeronautical applications. Being fully compatible of the reactive flow formulation of the cell-vertex solver AVBP, this study paves the way to future monolithic simulations of airblast injectors for aeronautical combustion chambers, including both the multi-phase and the reactive regions.

*Keywords:* Two-phase flow, airblast, diffuse interface, hyperbolic systems

---

## 1. Introduction

Liquid injection and atomization are complex processes which are at the heart of many industrial systems. In the context of combustion, these phenomena play a key role as they drive the fuel vapour distribution in a combustion chamber [1, 2], and therefore have a major impact on the flame regime and burner efficiency, as well as pollutant emissions [3]. In addition, fuels are blends of numerous molecules, their exact composition being usually unknown. For example Shastry et al. [4] highlighted the preferential evaporation effect on the structure and propagation speed of spray flames. For these complicated problems numerical simulation represents a convincing approach to supplement

---

\*Corresponding author

*Email address:* peden@cerfacs.fr (Benoît Pédén)

<sup>1</sup>New address: CORIA, CNRS UMR6614, INSA and University of Rouen, Avenue de l'Université, 76801 Saint-Etienne-du-Rouvray, France

experiments. However, atomization is numerically challenging due to the large range of physical scales involved in this multi-physics problem, from the surrounding gas flow to the molecular scale at the interface between liquid and gas phases, considered as a discontinuity for viscosity and density, and consequently requiring specific numerical treatment.

For this reason, a strategy often used in complex industrial systems is to directly inject a train with prescribed droplet velocities and diameter size distribution [5, 6]. Such spray injection models have allowed successful spray flame simulations in both academic and realistic combustion chambers [7–10]. However, they require input parameters which are not always known and they suffer from a lack of physics of atomization, which prevent the spray formation to adapt to the flow.

Several approaches have been proposed in the literature to numerically predict the primary atomization of liquid jets or sheets by modelling the interface between liquid and gaseous phases, which can be split into two main categories: sharp and diffuse interface methods. Sharp interface methods consider the interface between the phases as a discontinuity in a way that flow variables experience a jump in their values. The material interface is tracked by the Front-Tracking methods [11–13] or captured using methods such as the Volume-Of-Fluid (VOF) method [14], or the Level-Set method [15]. These approaches are able to finely predict the evolution of the interface topology and its primary breakup [16–19]. However they require significant mesh resolution in the interface vicinity [20] which makes them unsuitable for prediction in complex industrial systems. In addition they are usually restricted to incompressible flows, i.e., not directly applicable to combustion. Diffuse interface methods (DIM) do alleviate these issues, with considering the interface as a transition region between the phases instead of a discontinuity, thus relaxing the mesh resolution constraints. To do so, they rely on unified equations of state describing both phases. Two sub-groups of DIM arise from the literature: the Phase-Field (PF) and the Multi-Fluid (MF) methods. PF methods are based on the early works of Van der Waals [21], Korteweg [22] and Cahn and Hilliard [23] to describe the Gibbs potential in the diffuse interface region. The concept is to track the phases with a dedicated field function and to solve each phase independently. Numerous Lattice-Boltzmann numerical formulations rely on this approach, allowing interesting applications for atomization in a incompressible context [24–27]. For compressible finite-volume or finite-element approaches, the second gradient theory [28] recently allowed to handle high density ratio in academic configurations [29]. MF methods rather consider the interface region as a mixture of phases, obeying a single set of equations. Several equilibrium hypotheses have been proposed to reduce the number of equations, from the general 7-equation formulation of Baer and Nunziato [30], to a reduced 5-equation formulation assuming pressure equilibrium [31–34], and down to a so-called homogeneous 4-equation formulation, assuming the mechanical and thermal equilibrium between phases [35]. Because they involve a only set of conservative equations to describe both phases, without tracking the interface, DIM relax the resolution constraint of sharp methods. Convex thermodynamic models [36] are used to close the equation set, such

as the Stiffened-Gas [37] or cubic equations of state, as recently proposed in several works [38]. Multi-Fluid methods allow the simulation of compressible, high density ratio industrial configurations at a reasonable computational cost. They were used in liquid rocket engine applications [39] using cubic [38, 40–42] or Stiffened-Gas equations of state [35, 43–45], or in Diesel injection setups with interesting results [46–48]. Contrary to PF approach, existing MF works have mainly neglected surface tension forces, which play a key role in atomization [49]. Primary and secondary atomization and directly the droplets distribution in the combustion chamber are a consequence of the surface tension forces.

The present work intends to assess the accuracy and robustness of the homogeneous model (four-equation model [35]) to predict liquid-gas flow dynamics. A Noble-Abel Stiffened-Gas (NASG) equation of state is used to close the system and the Continuum Surface Force formalism [50] extended to a compressible formulation [51] is considered to account for surface tension forces. As recommended in [52], the vertex-centered HLLC-MUSCL Riemann solver [53] is used for a robust and accurate prediction of the high density ratio faced in the targeted applications. Finally, characteristic boundary conditions which are required for compressible flows, are adapted to NASG thermodynamics. The model is first validated on a series of academic test cases, and finally applied to liquid film dynamics in an airblast atomizer. A series of pressurized tests are conducted on the last application. It is to the authors knowledge the first time that such airblast applications are conducted with a diffuse interface method, and that pressure effects on the liquid-gas interface dynamics can be investigated under a compressible, eventually reactive formalism.

The paper is structured as follows. The transport equations and closure models are presented in Sec. 2, then the numerical scheme is described in Sec. 3. Validations for the characteristic boundary conditions, and the surface tension implementation are proposed in Sec. 4. Finally, the results for the target application are presented in Sec. 5. Average and instantaneous results are compared to existing correlations, and the effect of pressure injection is investigated.

## 2. Model description

### 2.1. The 4-equation model

Initially proposed to simulate evaporating, cavitating and boiling flows [35, 54–56], the homogeneous 4-equation model assumes a mechanical and thermal equilibrium between the phases. Mechanical and thermal equilibriums are always true in pure phase media. In a multi-phase mixture, they mean that no slip velocity exists between phases, both phases have the same temperature. This implies that the region where both phases coexist is small. Species composing the mixture occupy their own volume and share the same pressure whether they are in liquid or gas phase which is similar to Dalton’s law [43]. With this hypotheses, the 4-equation model considers a mono-component liquid ( $k = 1$ ) and a multi-component gas mixture ( $k = [2, \dots, N]$ ), distinguishing the liquid

100 species and its vapour as two different species. The equilibrium leads to the following variable definitions

$$\begin{cases} T &= T_k, \quad \forall k, \\ P &= P_k, \quad \forall k, \\ v &= 1/\rho = \sum_{k=1}^N Y_k v_k, \\ e &= \sum_{k=1}^N Y_k e_k. \end{cases} \quad (1)$$

The resulting 4 equations write

$$\frac{\partial \rho}{\partial t} + \nabla \cdot (\rho \mathbf{u}) = 0, \quad (2a)$$

$$\frac{\partial \rho \mathbf{u}}{\partial t} + \nabla \cdot (\rho \mathbf{u} \otimes \mathbf{u} + P \mathbf{I}) = 0, \quad (2b)$$

$$\frac{\partial \rho E}{\partial t} + \nabla \cdot ((\rho E + P) \mathbf{u}) = 0, \quad (2c)$$

$$\frac{\partial \rho Y_k}{\partial t} + \nabla \cdot (\rho Y_k \mathbf{u}) = 0, \quad (2d)$$

where  $Y_k$  represents the mass fraction of species  $k$ ,  $\rho$ ,  $\mathbf{u}$ ,  $P$  and  $E$  respectively denote the mixture density, the velocity, the pressure and the total mixture energy ( $E = e + \mathbf{u}^2/2$ ). The internal energy writes  $e$ . As the 4-equation  
 105 model governed by Sys. (2) does not contain any non-conservative term, it is fully conservative. This model is classified under the category of Multi-Fluid methods, which distinguishes from Phase-Field methods by its approach to interface thickness control. Unlike Phase-Field methods, the simulation does not actively manipulate the interface thickness. This deliberate choice is motivated  
 110 by the specific applications targeted by the model, where the flow dynamics are sufficiently fast to prevent excessive diffusion of the interface, and by the fact that Sys. (2) corresponds to the usual set of equations solved in combustion solvers [57].

## 2.2. Thermodynamic closure

115 A consistent Equation of State (EoS) must be used to correctly relate density, temperature and pressure of liquid and gas phases. This EoS should be able to reproduce the thermodynamic behaviour of species on a large range of temperatures and pressures.

As suggested by Le Métayer et al. [37], in the context of the 4-equation  
 120 model using a convex EoS for each phase allows to preserve the hyperbolicity of the Sys. (2) which simplifies its resolution. The liquid and its vapour are thus transported through two distinct equations [35] and mass-transfer between phases occurs assuming an instantaneous local thermodynamic equilibrium. When the conditions are far from the saturation, no phase change occurs and the local  
 125 thermodynamic equilibrium can be neglected. This is the case in this work, i.e., no evaporation/condensation are considered.

### 2.2.1. The Noble-Abel Stiffened-Gas equation of state

Cubic equations of state [58, 59] are good candidates to describe both phases but they loose convexity in the spinodal region of the Clapeyron diagram. The  
130 Noble-Abel Stiffened-Gas (NASG) equation of state [60] extends the popular Stiffened-Gas formulation which considers covolumes and expresses as for a given constituent  $k = [1, \dots, N]$  as

$$P_k = \frac{\rho_k(\gamma_k - 1)C_{v,k}T_k}{1 - \rho_k b_k} - P_{\infty,k}, \quad (3)$$

where  $\rho_k$ ,  $\gamma_k$ ,  $C_{v,k}$ ,  $b_k$  and  $P_{\infty,k}$  are respectively the density, the Laplace coefficient, the isovolume specific heat capacity, the covolume and the constant  
135 representing attractive effects in liquid phase: the gaseous phase relaxes to the ideal gas EoS with  $P_{\infty,k} = 0$  and  $b_k = 0$ .

Internal energy, enthalpy, entropy and the speed of sound read

$$e_k = \frac{P_k + \gamma_k P_{\infty,k}}{P_k + P_{\infty,k}} C_{v,k} T_k + q_k, \quad (4)$$

$$h_k = \gamma_k C_{v,k} T_k + b_k P_k + q_k, \quad (5)$$

$$s_k = C_{v,k} \ln \left( \frac{T_k^{\gamma_k}}{(P_k + P_{\infty,k})^{\gamma_k - 1}} \right) + q'_k, \quad (6)$$

$$c_k^2 = \frac{\gamma_k (P_k + P_{\infty,k})}{\rho_k (1 - \rho_k b_k)}, \quad (7)$$

where the two added constants  $q_k$  and  $q'_k$  respectively represent the reference energy and entropy of species  $k$ . The NASG EoS parameters are determined according the methodology proposed in Boivin et al. [61]. In order to avoid small  
140 time-steps induced by the CFL constraint in the liquid phase, these parameters are derived assuming a modified sound speed in the liquid phase, equal to the one of the gaseous phase [62].

### 2.2.2. Extension of NASG equation of state to multi-component gas mixtures

Extension of Sys. (1) to multi components gas has been proposed in Chiapolino et al. [43], and is reminded here for clarity. Writing Eq. (3) for each  
145 species with  $\rho_k = 1/v_k$ , the mixture temperature is easily retrieved

$$T(v, P, Y_k) = \frac{v - \sum_{k=1}^N Y_k b_k}{\sum_{k=1}^N Y_k \frac{(\gamma_k - 1) C_{v,k}}{P + P_{\infty,k}}}. \quad (8)$$

The mixture pressure is then obtained by rewriting Eq. (8), yielding a quadratic form

$$P = \frac{b + \sqrt{b^2 + 4ac}}{2a}, \quad (9)$$

with

$$\begin{cases} a = v - Y_1 b_1, \\ b = \sum_{k=1}^N Y_k (\gamma_k - 1) C_{v,k} T - P_{\infty,1} (v - Y_1 b_1), \\ c = \sum_{k>1}^N Y_k (\gamma_k - 1) C_{v,k} P_{\infty,1} T. \end{cases} \quad (10)$$

150 Note that a proof of the pressure positivity was presented by Chiapolino et al. [43], and that the formula is only valid if a single liquid component is present (here,  $k = 1$ ).

Finally density and internal energy are computed through Eqs. (3) and (4) according to Sys. (1)

$$\frac{1}{\rho} = \sum_{k=1}^N Y_k \left( \frac{(\gamma_k - 1)C_{v,k}T}{P + P_{\infty,k}} + b_k \right), \quad (11)$$

$$e = \sum_{k=1}^N Y_k \left( \frac{P + \gamma_k P_{\infty,k}}{P + P_{\infty,k}} C_{v,k}T + q_k \right). \quad (12)$$

### 2.3. Jacobian flux matrix $\mathcal{E}$ boundary conditions

Characteristic boundary conditions [63] are required in a compressible context to be consistent with the system of waves travelling inside the computational domain. The Locally One-Dimensional Inviscid flow (LODI) hypothesis introduced by Thompson [64] is considered. Following Okong'o and Bellan [65], characteristic formulations must be adapted when using non-perfect equation of state. Pelletier et al. [38] have derived the characteristic formulation for a 4-equation model, closed with a cubic equation of state. A similar exercise is conducted here, for the NASG equation of state. The computation of coefficients  $\Lambda$  and  $\Gamma$  involved in the Jacobian fluxes matrix as well as the speed of sound are detailed in Appendix A,

$$\Lambda = \left. \frac{\partial P}{\partial \rho e} \right|_{\rho Y_k} = \frac{1}{\frac{\rho \bar{C}_p \beta}{\alpha} - \alpha T}, \quad (13)$$

$$\Gamma = \left. \frac{\partial \rho e}{\partial \rho Y_k} \right|_{P, Y_{i \neq k}} = h_k - \frac{\rho \bar{C}_p}{\alpha \rho_k}, \quad (14)$$

with  $\alpha$  and  $\beta$  respectively the isobaric dilatation and isotherm compressibility coefficients. The mean isobaric heat capacity is defined as  $\bar{C}_p = \sum_k Y_k C_{pk}$ .

### 2.4. Additional terms: surface tension $\mathcal{E}$ viscous term

Surface tension is accounted for following the methodology proposed by Brackbill et al. [50], taking the liquid volume fraction  $\alpha_l$  as the continuous color function. The resulting force  $\mathbf{F}_\sigma$  yields

$$\mathbf{F}_\sigma = \sigma \kappa \nabla \alpha_l, \quad (15)$$

160 with  $\sigma$  the surface tension coefficient and  $\kappa$  the local curvature defined as

$$\kappa = - \nabla \cdot \left( \frac{\nabla \alpha_l}{|\nabla \alpha_l|} \right). \quad (16)$$

This formulation of the surface tension force enables a fast and computationally efficient integration of capillary effects into the system of equations. In addition to

extending the method to compressible cases, Perigaud and Saurel [51] formulated the equation system in conservative form, offering improved accuracy in capturing capillary phenomena. However, the implementation of this formulation poses certain challenges, as outlined below:

- (i) Modification of the energy equation. A surface tension potential energy  $\mathcal{E}_\sigma$  is added to the conservative energy variable  $E$ . This potential energy term is defined as

$$\rho\mathcal{E}_\sigma = \sigma\|\nabla\alpha_l\|. \quad (17)$$

The energy equation then reads,

$$\frac{\partial(E + \sigma\|\nabla\alpha_l\|)}{\partial t} + \nabla \cdot \left( (E + \sigma\|\nabla\alpha_l\| + P) \mathbf{u} - \sigma \left( \|\nabla\alpha_l\| \bar{\mathbf{I}} - \frac{\nabla\alpha_l \otimes \nabla\alpha_l}{\|\nabla\alpha_l\|} \right) \right). \quad (18)$$

- (ii) Impact on flux formulation and solver: the conservative momentum and energy formulations lead to modifications in the flux formulation, requiring adjustments in the Riemann solver and the Jacobian flux matrix.

Considering that the AVBP solver [66, 67] is primarily used for single-phase gas applications, where the focus is mainly on simplicity and flexibility of implementation, the non-conservative form of the equations is preferred. This choice enables easier integration of the code with the desired level of simplicity and flexibility, aligning with the solver's primary application requirements. The surface tension effects are incorporated into the numerical simulations using a non-conservative formulation. This approach, despite its departure from a fully conservative framework, yields satisfactory results in validation test cases. The implementation of the non-conservative formulation within the AVBP solver has proven to be straightforward and efficient. By adopting this approach, the AVBP solver, which primarily focuses on single-phase gaseous applications, benefits from the simplicity and flexibility offered by the non-conservative treatment of surface tension effects. It allows to successfully incorporate surface tension modeling, enabling the accurate representation of interfacial phenomena and enhancing the reliability of simulations in complex fluid dynamics scenarios. Although a fully conservative formulation is expected to give a more precise prediction of the capillary effects, the results presented later show that this simpler formulation yields reasonable results due to the diffuse nature of the interface.

The viscous stress tensor and the energy flux read

$$\bar{\bar{\tau}} = -\frac{2}{3} \nabla \cdot (\mathbf{u}) \mathbf{I} + 2\bar{\bar{\mathbf{S}}}, \quad (19)$$

$$\mathbf{q} = -\lambda \nabla T, \quad (20)$$

with  $\bar{\bar{\mathbf{S}}} = \frac{1}{2} (\nabla \mathbf{u} + \nabla \mathbf{u}^t)$ . The mixture dynamic viscosity  $\mu$  and the thermal diffusion coefficient  $\lambda$  are defined as in Deng and Boivin [45]. Using this formulation,



coefficients continuity is conserved across the interface,

$$\mu = \alpha_l \mu_l + \alpha_v \mu_v, \quad (21)$$

$$\lambda = \alpha_l \lambda_l + \alpha_v \lambda_v, \quad (22)$$

where  $\mu_l$  and  $\lambda_l$  are the dynamic viscosity coefficient and the thermal diffusion coefficient of the liquid phase and  $\mu_g$  and  $\lambda_g$  are the ones of vapour phase. The volume fractions are defined as  $\alpha_k = \rho Y_k / \rho_k$ . In this study since only one liquid species and a multicomponent gas mixture are considered,  $\alpha_l = \alpha_1$  and  $\alpha_g = \sum_{k=2}^N \alpha_k$ . In Eqs. (21) and (22),  $\mu_l$  and  $\lambda_l$  are assumed constant and independent on temperature. The gaseous viscosity  $\mu_g$  depends on temperature and its behaviour is modelled with Sutherland's law [68]. The thermal diffusion coefficient of gaseous phase is computed through the Prandtl number  $Pr$ ,  $\mu_g$  and the mean gaseous mass specific calorific capacity  $\bar{C}_{p,g}$ ,

$$\lambda_g = \frac{\mu_g \bar{C}_{p,g}}{Pr}, \quad (23)$$

with

$$\bar{C}_{p,g} = \frac{\sum_{k=2}^N Y_k C_{p,k}}{\sum_{k=2}^N Y_k}. \quad (24)$$

The complete system of equations with non-Euler terms, taking the surface tension force following [51], reads

$$\frac{\partial \rho}{\partial t} + \nabla \cdot (\rho \mathbf{u}) = 0, \quad (25a)$$

$$\frac{\partial \rho \mathbf{u}}{\partial t} + \nabla \cdot (\rho \mathbf{u} \otimes \mathbf{u} + P \mathbf{I}) = \mathbf{F}_\sigma + \nabla \cdot (\mu \bar{\bar{\tau}}), \quad (25b)$$

$$\frac{\partial \rho E}{\partial t} + \nabla \cdot ((\rho E + P) \mathbf{u}) = \mathbf{u} \cdot \mathbf{F}_\sigma + \nabla \cdot (\mu \bar{\bar{\tau}} \cdot \mathbf{u}) - \nabla \cdot \mathbf{q}, \quad (25c)$$

$$\frac{\partial \rho Y_k}{\partial t} + \nabla \cdot (\rho Y_k \mathbf{u}) = 0. \quad (25d)$$

### 3. Numerical scheme

A vertex-centered Riemann solver scheme has been developed at CERFACS [53], and added in the compressible, massively parallel and unstructured Large-Eddy-Simulation (LES) solver AVBP [66, 67], to numerically handle with robustness high density gradients. Initially intended for plasma applications, it is adapted here to solve the Sys. (2), in conjunction with the NASG equation of state. Appendix B presents the numerical solver HLLC [69] along with the second order MUSCL reconstruction. The Sweeby [70] slope limiter is used for the MUSCL procedure. The temporal integration is performed with a three-step Runge-Kutta (RK) algorithm, as in [71]. The non-Euler terms from Sys. (25) are computed with specific methodologies. In the capillary term the divergence is computed with a  $4\Delta$  methodology presented in [71, 72]. The viscous terms

are computed with a Finite Element  $2\Delta$  operator [71, 72] to dissipate small  
 215 wavelength diagonal modes that could appear. The validation of the Eulerian  
 part of Sys. (2) is presented in appendix Appendix B.3.

#### 4. Canonical validations

In the following, we successively validate:

- the surface tension implementation,
- 220 • boundary conditions.

##### 4.1. Surface tension validation

###### 4.1.1. Laplace law

Surface tension, taken into account thanks to Eq. (15), is validated in this  
 subsection thanks to several test cases. The Laplace law is first assessed, con-  
 sidering a  $\text{H}_2\text{O}$  liquid droplet of radius 5 mm, in an atmosphere of a gaseous  
 $\text{O}_2\text{-N}_2$  mixture. The initial species profiles are set with a hyperbolic tangent  
 function,  $\Phi$ , defined as,

$$\Phi(\phi(x, y)) = \frac{1}{2} \left( 1 + \tanh \left( \frac{2\phi(x, y)}{\varepsilon} \right) \right), \quad (26)$$

$$\rho(x, y) = \Phi(x, y) \rho_l + (1 - \Phi(x, y)) \rho_g, \quad (27)$$

$$Y_{\text{H}_2\text{O}}(x, y) = \frac{\Phi(x, y) \rho_l}{\rho(x, y)}, \quad (28)$$

$$Y_{\text{N}_2}(x, y) = \frac{1 - Y_{\text{H}_2\text{O}}(x, y)}{\mathcal{F} + 1}, \quad (29)$$

$$Y_{\text{O}_2}(x, y) = \mathcal{F} Y_{\text{N}_2}(x, y), \quad (30)$$

$$(31)$$

where  $\phi(x, y)$  reads

$$\phi(x, y) = r - \sqrt{(x - x_c)^2 + (y - y_c)^2}, \quad (32)$$

with  $r$  the droplet radius,  $\varepsilon$  the interface width,  $(x_c, y_c)$  the droplet center  
 225 coordinates, and  $\mathcal{F}$  the ratio between  $\text{O}_2$  and  $\text{N}_2$  in pure air. The densities  $\rho_l$   
 and  $\rho_g$  of pure liquid and pure gas, respectively, are determined with the NASG  
 equation of state. The domain is a square of 50 mm side. The mesh consists in a  
 $500 \times 500$  grid cells, and the surface tension coefficient is  $\sigma = 73 \times 10^{-3} \text{ N.m}^{-1}$ .  
 The theoretical pressure drop across the interface predicted by the Laplace law is

$$P_l - P_v = \Delta P = \frac{\sigma}{r} = 14.6 \text{ Pa}. \quad (33)$$

230 The results of the simulation is plotted against the theoretical profile obtained  
 with Eq. (33) in Fig. 1a, leading to a relative error of 0.5 %. The method

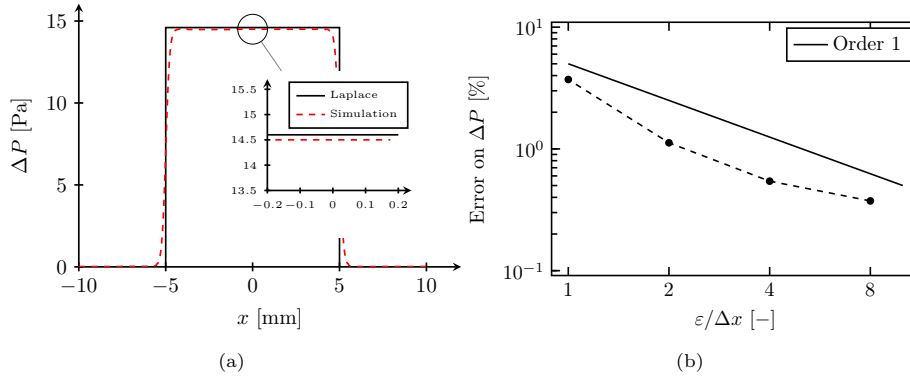


Figure 1: (a) Pressure difference profiles for simulation (red dashed line) and Laplace (black solid line). (b) Error on the Laplace pressure jump for different mesh resolutions. The liquid-gas interface width and the droplet radius are kept constant at  $\epsilon = 0.4$  mm and  $r = 5$  mm respectively.

employed to compute the error is based on the one adopted by [73], where it is computed in the all domain.

$$E_P = \frac{\sum_i \left| P(i) - \Phi \left( r - \sqrt{(x_i - x_c)^2 + (y_i - y_c)^2} \right) \frac{\sigma}{r} \right| V_i}{\sum_i \Phi \left( r - \sqrt{(x_i - x_c)^2 + (y_i - y_c)^2} \right) \frac{\sigma}{r} V_i}, \quad (34)$$

where  $P(i)$  is the pressure at node  $i$ ,  $\Phi(x, y)$  is the initial hyperbolic tangent,  $(x_i, y_i)$  are the coordinates of node  $i$  and  $V_i$  is the nodal volume. A mesh convergence study is conducted in Fig. 1b. The droplet radius  $r$  is kept at 5 mm and the initial interface width is kept constant at  $\epsilon = 0.4$  mm, representing 4 cells in the interface width for the case depicted by Fig. 1a (i.e. the cell size is  $\Delta x = 0.1$  mm). The numerical grid has been coarsen and refined to target 1 to 8 cells in the interface width  $\epsilon$ , by keeping it constant.

The performed simulations have demonstrated a clear relationship between mesh refinement and error reduction. As shown in Fig. 1b, the error level decreases linearly with finer mesh resolutions, indicating a first order convergent behavior.

#### 4.1.2. Oscillating droplet test case

The oscillation of an elliptic viscous droplet is then considered, as shown in Fig. 2. An elliptic shape droplet of radius  $a = 1.7$  mm and  $b = 1$  mm is initialized in a  $10 \times 10$  mm domain of air ( $O_2-N_2$ ) at rest. Simulations have been performed on a  $750 \times 750$  cells grid. The thermodynamic coefficients are given in Tab. 1. Thermodynamic features are  $P = 1$  bar,  $T = 293$  K and the surface tension coefficient is  $\sigma = 73 \times 10^{-3}$  N.m $^{-1}$ . The liquid and gaseous dynamic viscosities are respectively  $\mu_l = 0.854 \times 10^{-3}$  Pa.s and  $\mu_g = 1.72 \times 10^{-5}$  Pa.s.

Table 1: NASG thermodynamic coefficients for H<sub>2</sub>O (liquid), O<sub>2</sub>, N<sub>2</sub> species. Determined with NIST reference [74] with Boivin et al. [61] methodology.

Coefficients	H <sub>2</sub> O (liquid)	O <sub>2</sub>	N <sub>2</sub>
$C_{p,k}$ [J.kg <sup>-1</sup> .K <sup>-1</sup> ]	4185	919	1045
$C_{v,k}$ [J.kg <sup>-1</sup> .K <sup>-1</sup> ]	4180	650	742
$P_{\infty,k}$ [Pa]	$1.026 \times 10^7$	0	0
$q_k$ [J.kg <sup>-1</sup> ]	$-7.8998 \times 10^5$	$-2.104 \times 10^3$	$-2.355 \times 10^3$
$b_k$ [m <sup>3</sup> .kg <sup>-1</sup> ]	$9.2 \times 10^{-4}$	0	0

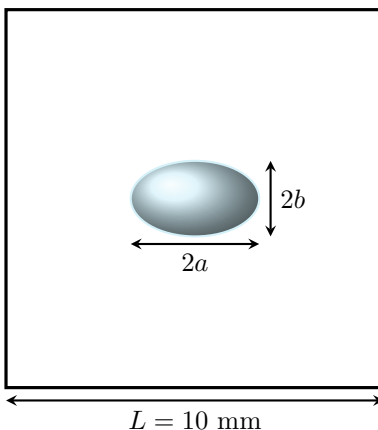


Figure 2: Oscillating droplet test case initialization. Dimensions  $2a$  and  $2b$  are respectively equal to 1.7 mm and 1 mm.

The initial species profiles are the same as in Sec. 4.1.1 but the  $\phi$  function is here replaced by

$$\phi(x, y) = 1 - \frac{x^2}{a^2} - \frac{y^2}{b^2} \quad (35)$$

255 where  $2a$  and  $2b$  are respectively the ellipse width and height, and  $\epsilon$  is the interface width.

The evolution of kinetic energy in the domain is shown in Fig. 3, evidencing its periodic evolution, damped by viscous forces. The normalized time  $t^*$  is defined as

$$t^* = \frac{t}{\sqrt{\frac{\rho_l r_{\text{eq}}^3}{\sigma}}}. \quad (36)$$

260 Theoretical studies have been proposed to predict the expected frequency of a 2D oscillating droplet. The work by Rayleigh [75], extended by Fyfe et al. [76] to account for surface tension predicts a pulsation

$$\omega^2 = (n^3 - n) \frac{\sigma}{(\rho_l + \rho_g) r_{\text{eq}}^3}, \quad (37)$$

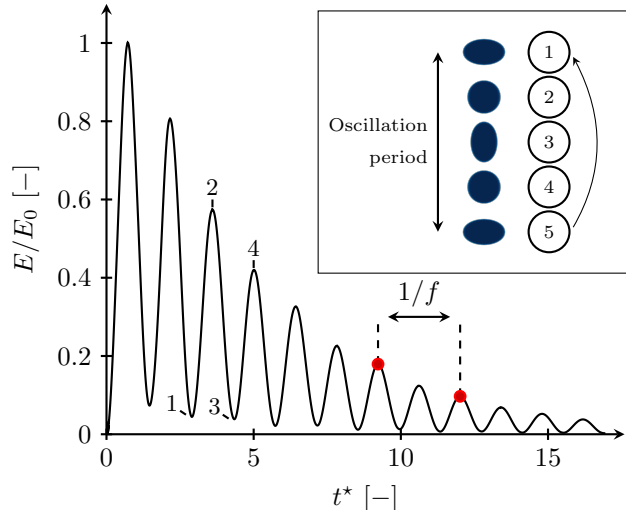


Figure 3: Time evolution of the kinetic energy in the domain and the corresponding droplet shapes from the simulation (density field).

where  $n = 2$  is the most unstable mode. The frequency reads

$$f = \frac{\omega}{2\pi}, \quad (38)$$

where  $r_{\text{eq}}$  is the equilibrium droplet radius. The numerical frequency is 73.03 Hz while the theoretical one computed with Eq. (38) is 71.61 Hz, resulting in 2 % relative error and falls in the range of previously reported simulations [51, 77].

#### 4.2. Boundary conditions validation

The Navier-Stokes Characteristic Boundary Condition (NSCBC) formalism for this two-phase framework is first assessed on the evacuation of an acoustic wave, superimposed to an  $\text{H}_2\text{O}-\text{O}_2$  mixture at rest, with  $Y_{\text{H}_2\text{O}} = 1 - Y_{\text{O}_2} = 0.98$ , which results in a liquid volume fraction  $\alpha_l = 7.55\%$ . Thermodynamic conditions are  $P_0 = 1$  atm and  $T_0 = 300$  K, and no artificial stabilization is applied. Gaussian forward and backward acoustic waves are superimposed. The left and right boundary conditions are outlet non-reflecting characteristic conditions [63]. Both HLLC-MUSCL [53] and a Two-step Taylor Galerkin (TTGC) scheme [78] are applied with CFL number 0.7. The use of the TTGC scheme is another validation as its formulation includes the Jacobian matrix and thus the thermodynamic specific terms, see Appendix A. Results are shown in Fig. 4, and evidence the fact that characteristic boundary conditions are able to properly handle acoustics without any reflection in this two-phase context.

The evacuation of a purely gaseous bubble from a pure liquid domain is also considered. This corresponds to the exit of an entropic wave. The test case consists in a pure  $\text{N}_2-\text{O}_2$  bubble, initialized in a pure  $\text{H}_2\text{O}^l$  domain of 1 m long,

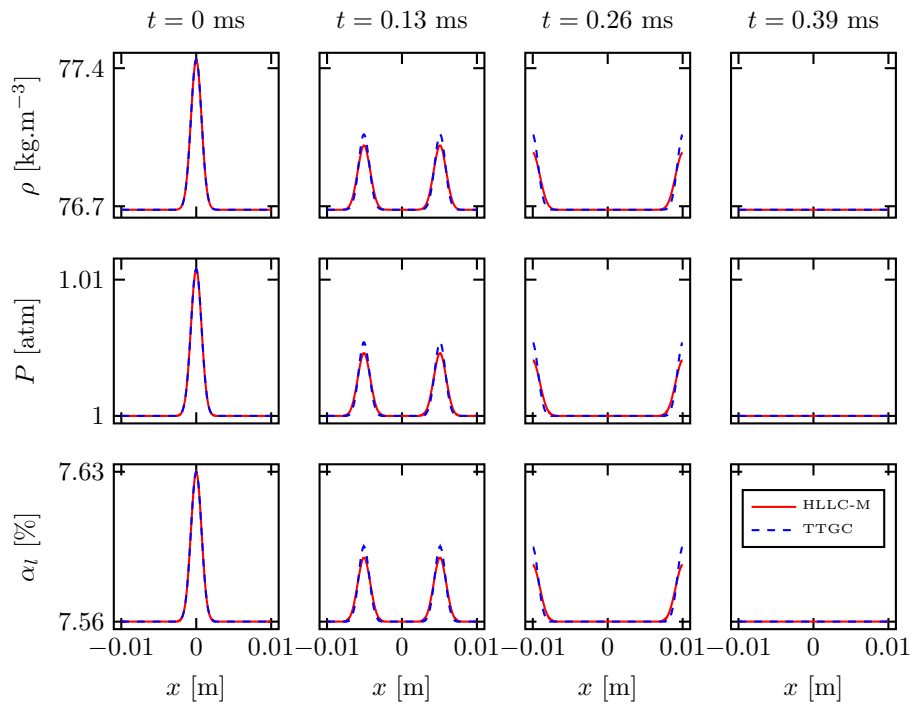


Figure 4: Superimposed backward and forward acoustic waves with fully non-reflecting boundary conditions. Red solid line: HLLC-MUSCL RK3 scheme [53], blue dashed line: TTGC scheme [78].

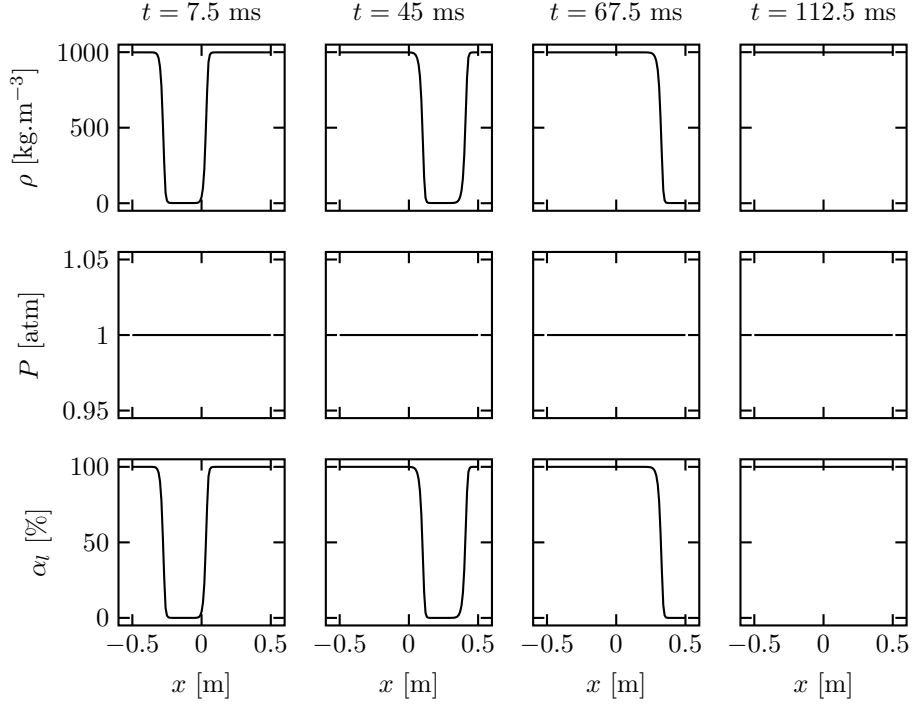


Figure 5: Air bubble in a liquid H<sub>2</sub>O environment transport to the outlet boundary condition.

discretized by 100 mesh nodes, with an initial velocity  $\mathbf{u}_0 = 10 \text{ m.s}^{-1}$ . The  
 285 thermodynamic conditions are  $P_0 = 1 \text{ atm}$ ,  $T_0 = 300 \text{ K}$ . The initial profile  
 of species across the interface follows Eqs. (27) to (30) but the  $\Phi$  function is  
 modified and reads

$$\Phi(x) = \frac{1}{2} \frac{1 + \tanh(\sqrt{6}(x + 0.3))}{4\Delta x} - \frac{1}{2} \frac{1 + \tanh(\sqrt{6}(x + 0.1))}{4\Delta x}, \quad (39)$$

where  $\Delta x$  is the cell size.

As shown in Fig. 5, the considered characteristic boundary condition allows to  
 290 correctly evacuate the gaseous bubble from the liquid domain without reflecting  
 waves.

#### 4.2.1. Water droplet advection to non-reflecting boundary condition

This section focuses on the convection of a two-dimensional droplet and  
 aims to investigate the interaction between a curved interface and the outlet  
 boundary condition. A pure liquid H<sub>2</sub>O droplet, initially traveling at a velocity  
 295 of  $\mathbf{u}_0 = 10 \text{ m.s}^{-1}$ , is placed in a pure N<sub>2</sub>-O<sub>2</sub> domain, with thermodynamic  
 conditions set to  $P_0 = 1 \text{ bar}$  and  $T_0 = 293 \text{ K}$ . The surface tension coefficient for  
 this system is  $\sigma = 73 \times 10^{-3} \text{ N.m}^{-1}$ . The domain is a square of 50 mm side.  
 The mesh consists in a  $1000 \times 1000$  grid cells.

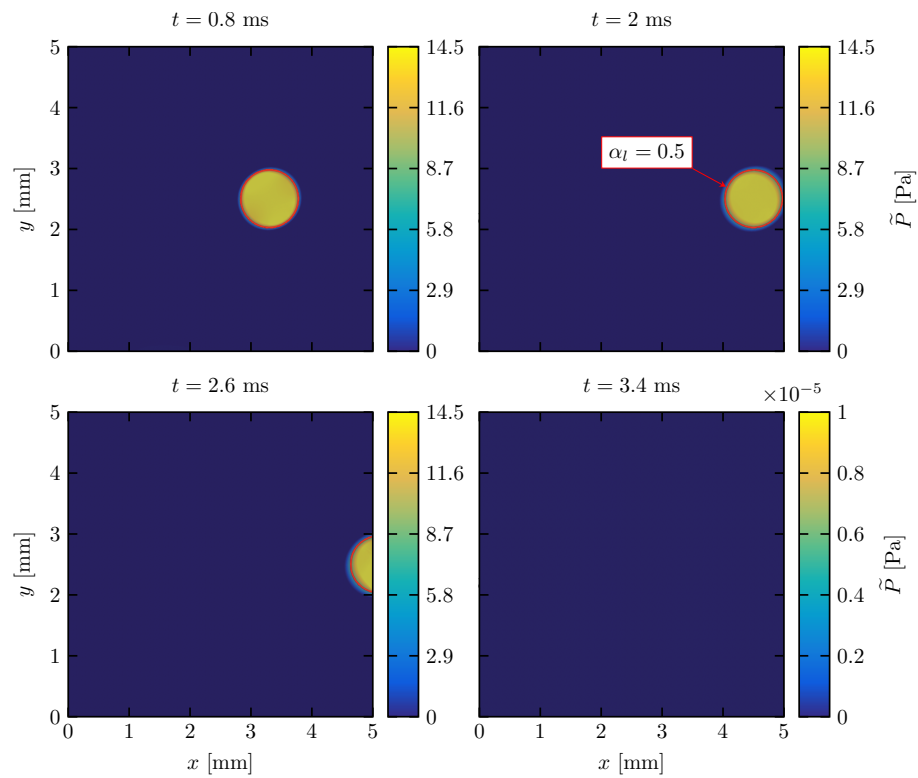


Figure 6: 2D liquid H<sub>2</sub>O droplet advection to the outlet boundary condition with  $\tilde{P} = P - P_0$ . The red circle is  $\alpha_l = 0.5$  isocontour. Note that the colorbar is rescaled for the last instant.



300 The results presented in Fig. 6 demonstrate that the droplet is evacuated without  
producing any reflecting waves.

## 5. Application: 2D Airblast liquid sheet

The intent of this section is to assess the implemented methodology on a  
practical configuration of interest for aircraft engines. Airblast atomization  
305 consists in a low-velocity liquid jet sheared by a faster gaseous co-flow. Such  
a configuration leads to the development of liquid ligaments which break into  
droplets [79]. It is of particular interest since liquid atomization is a key parameter  
for combustion quality in aeronautical or automotive applications. For this study,  
a configuration experimentally studied at the LEGI lab [80–85] is considered,  
310 where a liquid film injected at low velocity along a horizontal wall is sheared by  
a high-speed air stream.

Experimental and theoretical works [80–83] have shown that a primary  
instability develops due to a Kelvin-Helmholtz instability between the liquid and  
the gas, while a transverse Rayleigh-Taylor instability leads to the development  
315 of liquid ligaments. A linear stability analysis allows to predict the dominant  
axial wavelength  $\lambda_{\text{axi}}$  for the primary instability [79, 80, 82, 83] as

$$\lambda_{\text{axi}} = C_{\text{axi}} \sqrt{\frac{\rho_l}{\rho_g}} \delta_g, \quad (40)$$

where  $C_{\text{axi}}$  is a constant,  $\rho_l$  and  $\rho_g$  are respectively liquid and gas densities.  
The gas vorticity thickness  $\delta_g$  is computed using the experimental correlation  
established in [83]

$$\delta_g = \frac{6H_g}{\sqrt{Re_g}}, \quad (41)$$

320 where  $Re_g$  is the gaseous flow Reynolds number defined as

$$Re_g = \frac{\rho_g U_g H_g}{\mu_g}. \quad (42)$$

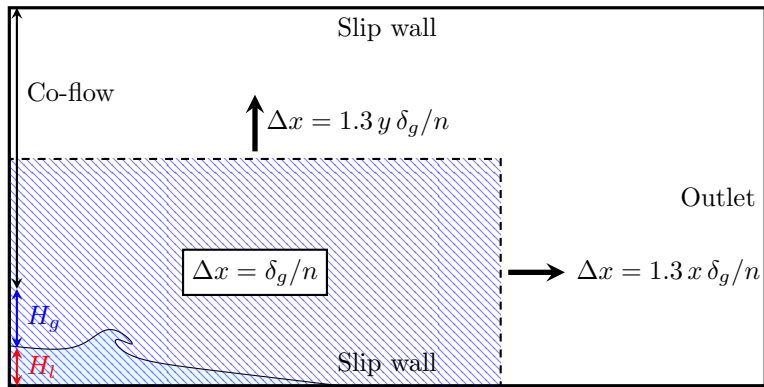
The velocity of the axial instability can be computed thanks to the Dimotakis  
velocity  $U_c$  [86] which has shown to be in very good agreement with measured  
wave velocities [80, 82]

$$U_c = \frac{\sqrt{\rho_g} U_g + \sqrt{\rho_l} U_l}{\sqrt{\rho_g} + \sqrt{\rho_l}}, \quad (43)$$

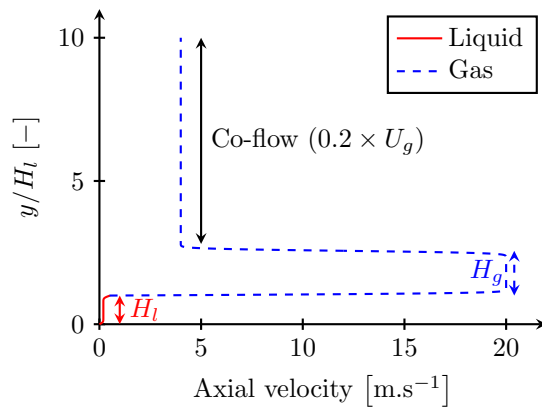
and finally the dominant axial frequency is

$$f_{\text{axi}} = \frac{U_c}{\lambda_{\text{axi}}}. \quad (44)$$

325 Several numerical studies have investigated this experimental configuration,  
relying on incompressible VOF methods in 2D [87–91] and in 3D [92]. Transversal  
instabilities are not taken into account in 2D simulations, but results showed a  
good quantitative agreement with experiments.



(a) Sketch and mesh discretization of the configuration.



(b) Inlet velocity profile. The blue dashed curve represents the gaseous flow while the solid red curve represents the liquid flow.

Figure 7: 2D Airblast configuration.

The computational domain considered in the present study consists in a  
 330  $20 H_l \times 10 H_l$  rectangular box, sketched in Fig. 7a. The numerical domain is  
 discretized with a cell size equal to  $\delta_g/n$  (with  $n = 2, 4$  and  $8$ ) near the injection  
 and shear zone ( $13 H_l \times 6 H_l$ ), and the mesh is stretched in both vertical and  
 axial directions outside of these regions. The geometric parameters considered in  
 our numerical simulation are the same as in the numerical work of Fuster et al.  
 335 [88], i.e., liquid and gas enter in the domain from left with heights respectively  
 equal to  $H_l = 6.4$  mm and  $H_g = 10$  mm, as shown in Fig. 7a. The considered  
 species are liquid water  $H_2O^l$  for liquid flow and respectively 22 % and 78 %  
 in mass of oxygen  $O_2^v$  and nitrogen  $N_2^v$  for the gaseous flow, and the surface  
 tension coefficient is  $\sigma = 69 \times 10^{-3}$  N.m<sup>-1</sup>. Following Bozonnet et al. [91], no  
 340 splitter separating plate is considered and continuous profiles are imposed at the  
 inlet, as illustrated in Fig. 7b. The inlet velocity profile is given by Eqs. (45)  
 to (47):

$$u(y) = \left[ U_l \operatorname{erf} \left( \frac{H_l - y}{\delta_l} \right) + U_i \left( 1 + \operatorname{erf} \left( \frac{y - H_l}{\delta_l} \right) \right) \right] \times \operatorname{erf} \left( \frac{y}{\delta_l} \right), \quad (45)$$

for  $y \leq H_l$ .

$$u(y) = \left[ U_g \operatorname{erf} \left( \frac{y - H_l}{\delta_g} \right) + U_i \left( 1 - \operatorname{erf} \left( \frac{y - H_l}{\delta_l} \right) \right) \right] \\ \times \operatorname{erf} \left( \frac{H_g + H_l - y}{\delta_g} \right) + U_{sm} \left( 1 + \operatorname{erf} \left( \frac{y - (H_g + H_l)}{\delta_g} \right) \right), \quad (46)$$

for  $H_l < y \leq H_g + H_l$ .

$$u(y) = U_{sm} \left( 1 - \operatorname{erf} \left( \frac{y - (H_g + H_l)}{\delta_g} \right) \right) + U_{cf} \operatorname{erf} \left( \frac{y - (H_g + H_l)}{\delta_g} \right), \quad (47)$$

345 for  $y > H_g + H_l$ ,  
 where  $\delta_g$  is the gas vorticity thickness,  $\delta_l$  the liquid vorticity thickness,  $U_i =$   
 $\delta_l (U_g \mu_g / \delta_g + U_l \mu_l / \delta_l) / (\mu_l + \mu_g)$  is the interfacial velocity defined in [93],  $U_{cf} =$   
 $0.2 U_g$  is the co-flow velocity and  $U_{sm} = (U_{cf} + U_g) / 2$  is the gaseous phase mixing  
 layer velocity. Liquid and gaseous dynamic viscosities are respectively denoted  
 350  $\mu_l$  and  $\mu_g$ .

At the initial state the domain is at rest with temperature  $T = 300$  K. The  
 air flow is fixed at  $U_g = 20$  m.s<sup>-1</sup> and liquid velocity is computed to reach a  
 dynamic pressure ratio  $M = (\rho_g U_g^2) / (\rho_l U_l^2) = 16$  resulting in  $U_l = 0.1735$  m.s<sup>-1</sup>  
 at  $P = 1$  bar. The simulation parameters are given in Tab. 2, and species  
 355 properties are the ones considered in the validation test-cases Tab. 1, for which  
 the liquid water species has a modified sound speed, resulting in a slightly  
 modified density ( $\rho_l = 939$  kg.m<sup>-3</sup> at 1 bar). Imposed inlet velocity values are  
 kept constant in the study. An air co-flow is added on top of the high-speed air  
 stream similarly as [92], to limit gaseous recirculations in this region. Inlet and  
 360 outlet boundary conditions are characteristic non-reflecting boundary conditions,  
 validated above in Sec. 4.2 for the current framework.

Table 2: Simulation parameters:  $U$  is the velocity,  $\mu$  is the dynamic viscosity and  $\sigma$  is the surface tension coefficient.

Phase	$U$ [m.s <sup>-1</sup> ]	$\mu$ [Pa.s]	$\sigma$ [N.m <sup>-1</sup> ]
Liquid	0.1735	$1 \times 10^{-3}$	$69 \times 10^{-3}$
Gas	20	$1.8 \times 10^{-5}$	–

An instantaneous density field is shown in Fig. 8a, evidencing the development of liquid ligaments. In order to quantitatively assess the results, the liquid core length predicted by the correlation of Raynal [80] is reported with a thick orange line. This correlation provides the intact liquid core length  $L$  thanks to Eq. (48),

$$L = \frac{12 H_l}{\sqrt{M}}, \quad (48)$$

and is retrieved from previous numerical works relying on sharp interface methods [77, 89, 90]. Mean profiles of liquid volume fraction  $\alpha_l = 0.1, 0.5$  and  $0.9$  are given in Fig. 8b for the three mesh resolutions ( $n = 2, 4$  and  $8$ ). The intact liquid core more likely corresponds to the iso-contour  $\alpha_l = 0.9$ , and Fig. 8b shows that increasing mesh resolution allows to obtain a fair agreement with the experimental correlation of Raynal Eq. (48). Figure 8c shows the  $\alpha_l = 0.5$  isocontour evolution for the resolution  $n = 8$  during 400 ms, corresponding to the passage of approximately 10 waves. The liquid sheet oscillates above the experimental correlation of Raynal [80] and the film height decreases following the slope of Eq. (48) given by the thick black line. The accurate prediction of this liquid core length shows the ability of the diffuse interface method to predict the liquid entrainment within the two-phase mixing layer.

The normalized amplitude spectrograms ( $\mathcal{A}^*$ ) of the interface height for  $P = 1$  bar with different mesh resolutions are given in Fig. 9a ( $\Delta x = \delta_g/n$  with  $n$  given on Fig. 9a), at position  $x = 2 H_l$ . These spectra have been obtained with the Welch method [94] to extract the most amplified frequency. The signal is divided into ten segments with a 60 % overlap as in Bozonnet et al. [91], and the liquid volume fraction is integrated across vertical lines to determine the liquid height. This process is repeated for multiple axial positions ranging from 0 to 13 times the liquid injection height  $H_l$ . Afterwards, the signals undergo Fast Fourier Transform (FFT), and the results are averaged. Despite an increase of numerical noise the main frequency remains the same for the three meshes, meaning that independence from mesh resolution is reached. The signal is processed for a time  $t$  so that the number of generated waves is larger than 30 ( $\tau = f\Delta t$ ). Bozonnet et al. [91] showed that even  $\tau \approx 10$  is enough to obtain a good estimate of the frequency. The value found is  $f = 24$  Hz which is equivalent to a Strouhal number  $St = f\delta_g/U_g = 6.5 \times 10^{-4}$ . The value is compared in Tab. 3 with previous studies at the same operating point and falls in the range of reported Strouhal numbers meaning that the essential instability mechanisms are captured by the method.

The resolution  $n = 2$  is adopted for the rest of the study to keep reasonable computational costs. Further simulations are finally conducted to investigate new

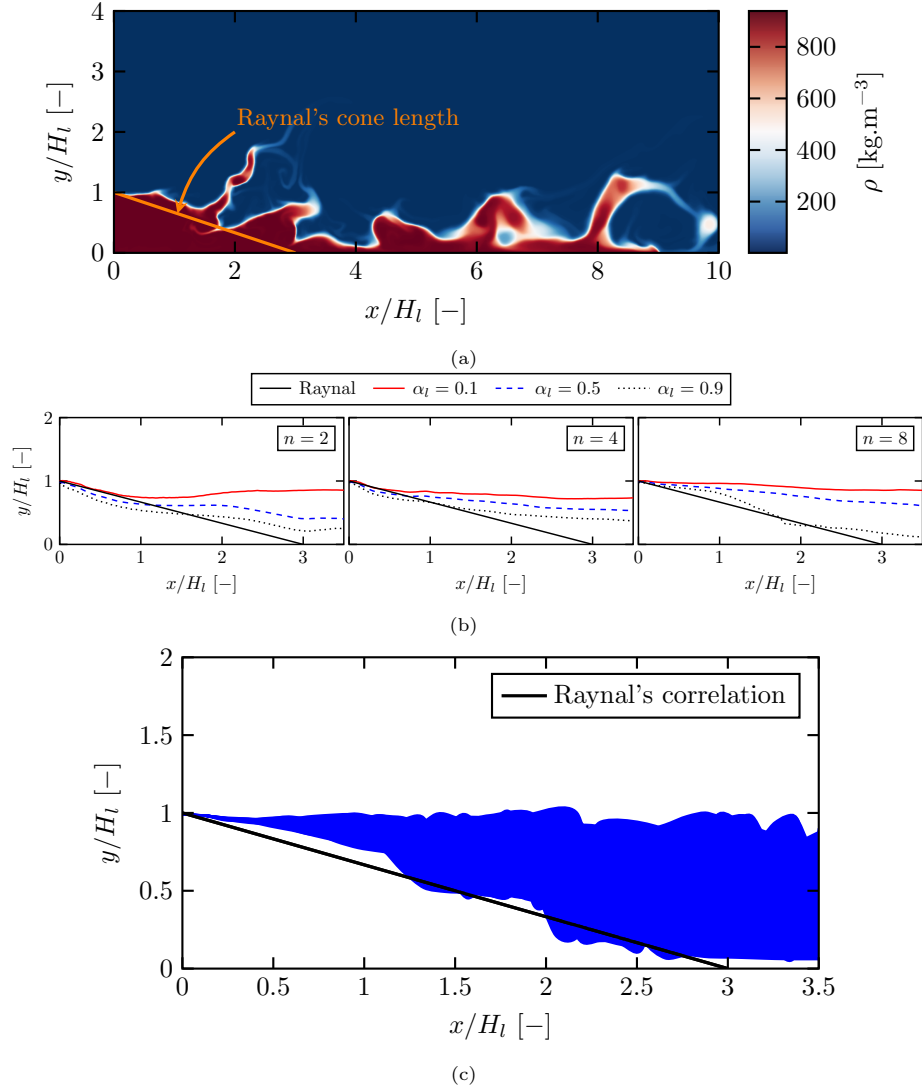
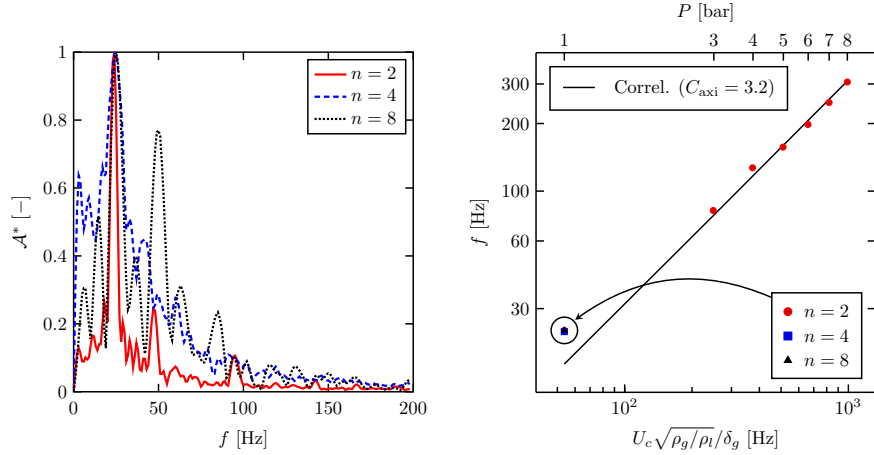


Figure 8: (a) Instantaneous density field. The thick orange line represents the intact cone length of Raynal [80]. (b) Liquid volume fraction mean profiles ( $\alpha_l = 0.1, 0.5$  and  $0.9$ ) for the three resolutions used ( $n = 2, 4$  and  $8$ ) compared to the correlation of Raynal Eq. (48) (black solid line). (c) Comparison of the liquid cone length at  $P = 1$  bar. The thick black line represents the the correlation length of Eq. (48). The blue area represents 40 isocontours of  $\alpha_l = 0.5$  over 400 ms with  $n = 8$  resolution representing the area swept by the liquid sheet interface.

Table 3: Comparison of previous experimental and numerical values of Strouhal numbers with the present study for the case  $M = 16$  and  $P = 1$  bar.

	Strouhal ( $\times 10^{-4}$ )
Raynal [80] (exp.)	6
Marmottant and Villermaux [79] (exp.)	7.5
Ben Rayana [82] (exp.)	7.6
Matas et al. [83] (exp.)	5
Fuster et al. [88] (VOF simulation – exp.)	8 – 5
Agbaglah et al. [89] (VOF simulation)	5.3
Present study	6.5



(a) Normalized amplitudes  $\mathcal{A}^*$  for  $P = 1$  bar. (b) Main frequency as a function of the pressure and the quantity  $U_c \sqrt{\rho_g / \rho_l} / \delta_g$ .

Figure 9: Results of the spectral analysis. (a) Normalized amplitude  $\mathcal{A}^*$  of the Fast Fourier Transform (FFT) at  $P = 1$  bar for different mesh resolutions at position  $x = 2 H_l$  and  $\tau \geq 30$ . (b) Main frequency evolution with pressure. The solid line represents the frequencies obtained with correlations Eqs. (40) and (44).

Table 4: Liquid and vapour densities for each pressure and the associated momentum ratio  $M$ .

Pressure [bar]	3	4	5	6	7	8
Liquid density $\rho_l$ [kg.m <sup>-3</sup> ]	941.6	942.8	943.9	945.1	946.2	947.3
Vapour density $\rho_g$ [kg.m <sup>-3</sup> ]	3.4	4.5	5.7	6.8	7.9	9.1
Momentum ratio $M$ [-]	48	64	80	95	111	127

operating ranges, hardly reachable with both experiments and incompressible solvers. Simulations are performed with various density ratios by adapting the pressure imposed at the outlet. The densities for each pressure are given in Tab. 4. The gas vorticity thickness  $\delta_g$  is adapted to the operating points in Eqs. (46) and (47) according to Eq. (41). Simulation parameters in Tab. 2 are kept constant. Results for the main frequency at various pressures are given in Fig. 9b and are compared to the one obtained from correlation Eq. (44) (black solid line) where a prefactor  $C_{\text{axi}} = 3.2$  is considered. The same methodology as in Fig. 9a has been used, however for  $P = 7$  and 8 bar raw FFT are considered because of a gas recirculation at the end of the liquid cone length. This phenomenon has also been experimentally observed by Raynal [80], Ben Rayana [82] for large momentum ratios, typically  $M > 100$ . Note that several values for  $C_{\text{axi}}$  can be found in literature. Raynal [80] proposed  $C_{\text{axi}} = 4$ , Ben Rayana [82] proposed  $C_{\text{axi}} = 1.5$  to 1.8. It has been shown that the different methodologies considered to experimentally measure the frequency can be a reason for these different values of  $C_{\text{axi}}$  [83]. Despite this uncertainty, linear stability analysis [80] predicts a linear relation between  $f$  and  $U_c \sqrt{\rho_g/\rho_l}/\delta_g$ , that is perfectly found in our simulations as pressure increases (Fig. 9b). It is to the authors' knowledge a rare confirmation of this theoretical prediction on a practical case.

Normalized amplitude spectrograms over a distance  $x/H_l = 8$  are given in Fig. 10. For each operating pressure point the main axial frequency is clearly visible near the injection. The frequency decreases downstream of a length approximately equal to the intact liquid cone length given by Eq. (48) highlighted with a solid black line in Fig. 10.

This finally shows that the sheared liquid-gas interface dynamics is well reproduced by the present method. The intact liquid core length is correctly retrieved, and the frequency evolution with pressure theoretically predicted by linear stability analysis is confirmed by our numerical approach. This methodology can therefore be considered with confidence for pressurized airblast configurations in future studies.

## 6. Conclusions

This paper presents first a validation of implemented methods for handling two-phase flow configurations in a fully compressible vertex-centered framework, utilizing a diffuse-interface Multi-Fluid method and a 4-equation model closed with a Noble-Abel Stiffened-Gas equation of state.

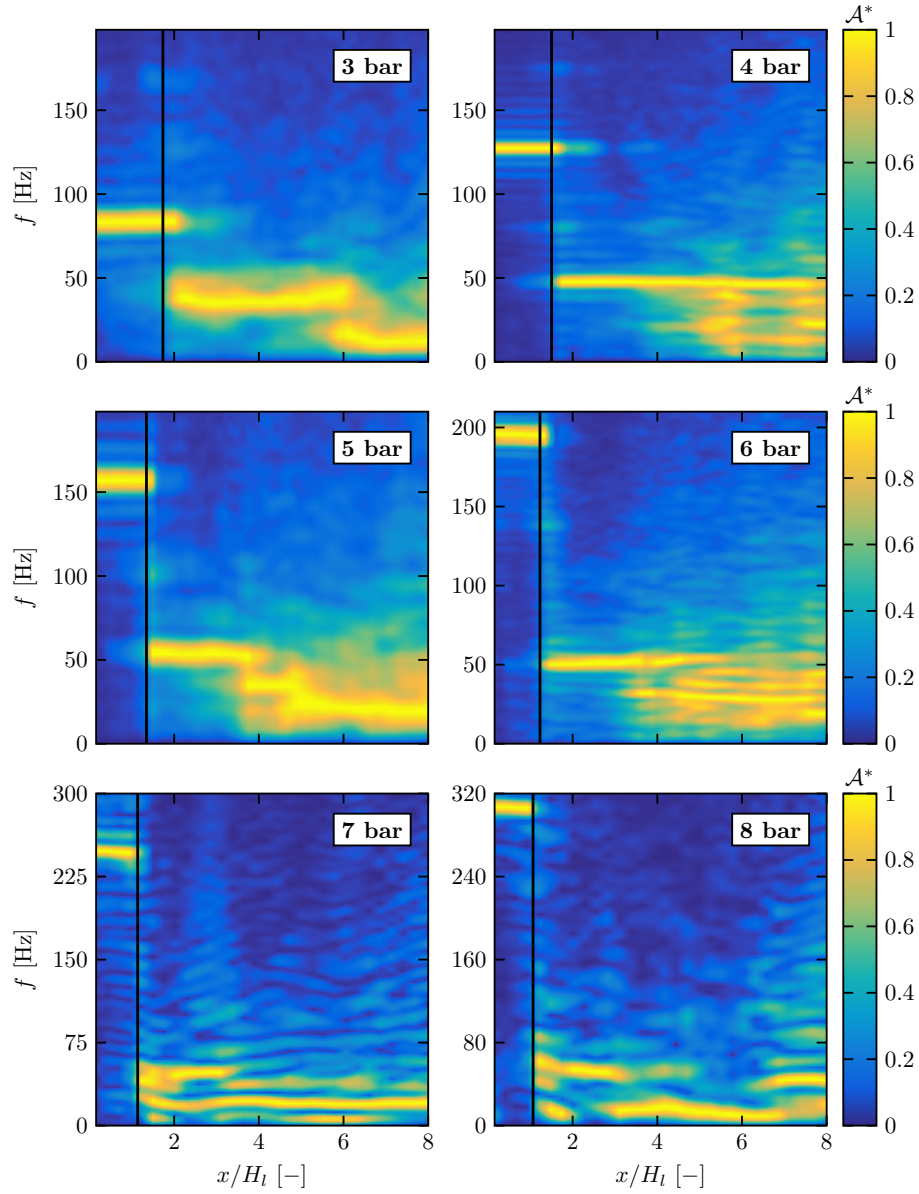


Figure 10: Amplitude normalized spectrograms ( $\mathcal{A}^*$ ) of interface height for  $P = 3$  to 8 bar over a distance  $x/H_l = 8$ . The solid black line represents the intact cone length from Eq. (48).



The vertex-centered HLLC-MUSCL numerical scheme has been implemented and validated on a number of academic test cases, demonstrating its ability to properly handle contact lines, shocks, and rarefaction waves. Additionally, the method effectively handles acoustics in the context of two-phase flow. Jacobian fluxes have been properly derived to allow the use of non-reflecting characteristic boundary conditions in conjunction with the NASG EoS. The non-reflectivity is assessed for both 1D and 2D two-phase test-cases. Capillary terms associated with the liquid-gas interface have been validated on simple configurations, with satisfactory results.

The methodology is then assessed on an air-assisted atomization configuration, for which experimental, theoretical, and numerical results can be found in the literature. Our results show the ability of the diffuse interface method to predict the intact liquid core length, as well as the interface dynamics. Furthermore, the methodology allows to investigate new operating ranges, and the effect of pressure increase on the primary interfacial wave frequency is studied. Our results show a very good agreement with the theoretical prediction of Raynal [80].

This allows to bridge the gap between usually incompressible methods considered for primary atomization, and compressible methods considered for prediction of combustion. Future work will be devoted to the development of a phase-change methodology, along with temperature-variable heat capacities, to properly handle reactive conditions. In addition, a coupling with a disperse spray Lagrangian model will be investigated, to allow a proper spray prediction in a realistic pressurized and reactive environment.

## Acknowledgments

BP is respectively grateful to Jérôme Dabas and Thibault Gioud for fruitful discussions about signal processing and Multi-Fluid methods. This work was supported by the French National Research Agency through the project MADIRAN (grant ANR-21-CE50-0043) and benefited from GENCI-CINES HPC resources (grant 2022 – A0112B10157).

## References

- [1] J. Réveillon, L. Vervisch, Analysis of weakly turbulent dilute-spray flames and spray combustion regimes, *Journal of Fluid Mechanics* 537 (2005) 317–347.
- [2] K. Luo, H. Pitsch, M. Pai, O. Desjardins, Direct numerical simulations and analysis of three-dimensional n-heptane spray flames in a model swirl combustor, *Proceedings of the Combustion Institute* 33 (2011) 2143–2152.
- [3] C. Beck, R. Koch, H.-J. Bauer, Identification of droplet burning modes in lean, partially prevaporized swirl-stabilized spray flames, *Proceedings of the Combustion Institute* 32 (2009) 2195–2203.

- 475 [4] V. Shastry, Q. Cazeres, B. Rochette, E. Riber, B. Cuenot, Numerical study of multicomponent spray flame propagation, *Proceedings of the Combustion Institute* 38 (2021) 3201–3211.
- [5] J. Senoner, M. Sanjosé, T. Lederlin, F. Jaegle, M. García, E. Riber, B. Cuenot, L. Gicquel, H. Pitsch, T. Poinso, Eulerian and Lagrangian Large-Eddy Simulations of an evaporating two-phase flow, *Comptes Rendus Mécanique* 337 (2009) 458–468.
- 480 [6] M. Sanjosé, J. Senoner, F. Jaegle, B. Cuenot, S. Moreau, T. Poinso, Fuel injection model for Euler–Euler and Euler–Lagrange Large-Eddy simulations of an evaporating spray inside an aeronautical combustor, *International Journal of Multiphase Flow* 37 (2011) 514–529.
- 485 [7] F. Shum-Kivan, J. M. Santiago, A. Verdier, E. Riber, B. Renou, G. Cabot, B. Cuenot, Experimental and numerical analysis of a turbulent spray flame structure, *Proceedings of the Combustion Institute* 36 (2017) 2567–2575.
- 490 [8] J. Tillou, J. Leparoux, J. Dombard, E. Riber, B. Cuenot, Evaluation and Validation of Two-Phase Flow Numerical Simulations Applied to an Aeronautical Injector Using a Lagrangian Approach, in: *Volume 4B: Combustion, Fuels, and Emissions*, American Society of Mechanical Engineers, 2020, p. 11. URL: <https://doi.org/10.1115/gt2020-15612>. doi:10.1115/gt2020-15612.
- 495 [9] E. L. Schiavo, D. Laera, E. Riber, L. Gicquel, T. Poinso, On the impact of fuel injection angle in Euler–Lagrange large eddy simulations of swirling spray flames exhibiting thermoacoustic instabilities, *Combustion and Flame* 227 (2021) 359–370.
- [10] V. Shastry, E. Riber, L. Gicquel, B. Cuenot, V. Bodoc, Large Eddy Simulations of complex multicomponent swirling spray flames in a realistic gas turbine combustor, *Proceedings of the Combustion Institute* (2022).
- 500 [11] J. Glimm, E. Isaacson, D. Marchesin, O. McBryan, Front tracking for hyperbolic systems, *Advances in Applied Mathematics* 2 (1981) 91–119.
- [12] S. Popinet, S. Zaleski, A front-tracking algorithm for accurate representation of surface tension, *International Journal for Numerical Methods in Fluids* 30 (1999) 775–793.
- 505 [13] G. Tryggvason, B. Bunner, A. Esmaeeli, D. Juric, N. Al-Rawahi, W. Tauber, J. Han, S. Nas, Y.-J. Jan, A Front-Tracking Method for the Computations of Multiphase Flow, *Journal of Computational Physics* 169 (2001) 708–759.
- [14] C. Hirt, B. Nichols, Volume of fluid (VOF) method for the dynamics of free boundaries, *Journal of Computational Physics* 39 (1981) 201–225.

- 510 [15] S. Osher, J. A. Sethian, Fronts propagating with curvature-dependent speed: Algorithms based on Hamilton-Jacobi formulations, *Journal of Computational Physics* 79 (1988) 12–49.
- [16] C. Pairetti, R. Villiers, S. Zaleski, On shear layer atomization within closed channels: Numerical simulations of a cough-replicating experiment, 515 *Computers & Fluids* 231 (2021) 105125.
- [17] J. Carmona, N. Odier, O. Desjardins, B. Cuenot, A. Misdariis, A. Cayre, A comparative study of direct numerical simulation and experimental results on a prefilming airblast atomization configuration, *Atomization and Sprays* 31 (2021) 9–32.
- 520 [18] A. A. Mukundan, T. Ménard, J. C. B. de Motta, A. Berlemont, Detailed numerical simulations of primary atomization of airblasted liquid sheet, *International Journal of Multiphase Flow* 147 (2022) 103848.
- [19] R. Janodet, C. Guillamón, V. Moureau, R. Mercier, G. Lartigue, P. Bénard, 525 T. Ménard, A. Berlemont, A massively parallel accurate conservative level set algorithm for simulating turbulent atomization on adaptive unstructured grids, *Journal of Computational Physics* 458 (2022) 111075.
- [20] C. I. Pairetti, S. M. Damián, N. M. Nigro, S. Popinet, S. Zaleski, Mesh resolution effects on primary atomization simulations, *Atomization and Sprays* 30 (2020) 913–935.
- 530 [21] J. D. Van der Waals, *Over de Continuïteit van den Gas-en Vloeïstoftoestand*, Ph.D. thesis, Sijthoff, 1873.
- [22] D. J. Korteweg, Sur la forme que prennent les équations du mouvement des fluides si l'on tient compte des forces capillaires causées par des variations de densité considérables mais continues et sur la théorie de la capillarité dans 535 l'hypothèse d'une variation continue de la densité, *Archives Néerlandaises de Sciences Exactes et Naturelles*, 1901.
- [23] J. W. Cahn, J. E. Hilliard, Free Energy of a Nonuniform System. I. Interfacial Free Energy, *The Journal of Chemical Physics* 28 (1958) 258–267.
- 540 [24] X. He, S. Chen, R. Zhang, A Lattice Boltzmann Scheme for Incompressible Multiphase Flow and Its Application in Simulation of Rayleigh–Taylor Instability, *Journal of Computational Physics* 152 (1999) 642–663.
- [25] H. W. Zheng, C. Shu, Y. T. Chew, Lattice Boltzmann interface capturing method for incompressible flows, *Physical Review E* 72 (2005).
- 545 [26] Y. Wang, C. Shu, J. Shao, J. Wu, X. Niu, A mass-conserved diffuse interface method and its application for incompressible multiphase flows with large density ratio, *Journal of Computational Physics* 290 (2015) 336–351.

- 550 [27] H. Liang, Y. Li, J. Chen, J. Xu, Axisymmetric lattice Boltzmann model for multiphase flows with large density ratio, *International Journal of Heat and Mass Transfer* 130 (2019) 1189–1205.
- [28] D. Jamet, O. Lebaigue, N. Coutris, J. Delhaye, The Second Gradient Method for the Direct Numerical Simulation of Liquid–Vapor Flows with Phase Change, *Journal of Computational Physics* 169 (2001) 624–651.
- 555 [29] D. Nayigizente, S. Ducruix, T. Schmitt, Development of an interface thickening method for the direct numerical simulation of compressible liquid–vapor flows in the framework of the second gradient theory, *Physics of Fluids* 33 (2021) 052119.
- [30] M. Baer, J. Nunziato, A two-phase mixture theory for the deflagration-to-detonation transition (ddt) in reactive granular materials, *International Journal of Multiphase Flow* 12 (1986) 861–889.
- 560 [31] A. Kapila, R. Menikoff, J. Bdzil, S. Son, D. Stewart, Two-phase modeling of deflagration-to-detonation transition in granular materials: Reduced equations, *Physics of Fluids* 13 (2001) 3002–3024.
- [32] G. Allaire, S. Clerc, S. Kokh, A Five-Equation Model for the Simulation of Interfaces between Compressible Fluids, *Journal of Computational Physics* 181 (2002) 577–616.
- 565 [33] A. Murrone, H. Guillard, A five equation reduced model for compressible two phase flow problems, *Journal of Computational Physics* 202 (2005) 664–698.
- 570 [34] R. Saurel, F. Petitpas, R. A. Berry, Simple and efficient relaxation methods for interfaces separating compressible fluids, cavitating flows and shocks in multiphase mixtures, *Journal of Computational Physics* 228 (2009) 1678–1712.
- [35] R. Saurel, P. Boivin, O. Le Métayer, A general formulation for cavitating, boiling and evaporating flows, *Computers & Fluids* 128 (2016) 53–64.
- 575 [36] R. Saurel, R. Abgrall, A Multiphase Godunov Method for Compressible Multifluid and Multiphase Flows, *Journal of Computational Physics* 150 (1999) 425–467.
- [37] O. Le Métayer, J. Massoni, R. Saurel, Elaboration des lois d’état d’un liquide et de sa vapeur pour les modèles d’écoulements diphasiques, *International Journal of Thermal Sciences* 43 (2004) 265–276.
- 580 [38] M. Pelletier, T. Schmitt, S. Ducruix, A multifluid Taylor-Galerkin methodology for the simulation of compressible multicomponent separate two-phase flows from subcritical to supercritical states, *Computers & Fluids* 206 (2020) 104588.
- 585

- [39] C. Le Touze, L.-H. Dorey, N. Rutard, A. Murrone, A compressible two-phase flow framework for Large Eddy Simulations of liquid-propellant rocket engines, *Applied Mathematical Modelling* 84 (2020) 265–286.
- 590 [40] P. Gaillard, V. Giovangigli, L. Matuszewski, A diffuse interface Lox/hydrogen transcritical flame model, *Combustion Theory and Modelling* 20 (2016) 486–520.
- [41] T. Gioud, N. Odier, B. Cuenot, T. Schmitt, D. Saucereau, M. Martin-Benito, Injection modelling in LOX/GCH<sub>4</sub> rocket engines with a diffuse interface method, in: *Space Propulsion Conference - 09-13 May, 2022*, p. 10.
- 595 [42] P. Tudisco, S. Menon, Numerical investigations of thermodynamic states formed near a reacting, supercritical CH<sub>4</sub>/O<sub>2</sub> flame, *Proceedings of the Combustion Institute* (2022).
- 600 [43] A. Chiapolino, P. Boivin, R. Saurel, A simple and fast phase transition relaxation solver for compressible multicomponent two-phase flows, *Computers & Fluids* 150 (2017) 31–45.
- [44] A. Chiapolino, R. Saurel, Extended Noble–Abel Stiffened–Gas Equation of State for Sub-and-Supercritical liquid-gas systems far from the critical point, *Fluids* 3 (2018) 48.
- 605 [45] X. Deng, P. Boivin, Diffuse interface modelling of reactive multi-phase flows applied to a sub-critical cryogenic jet, *Applied Mathematical Modelling* 84 (2020) 405–424.
- [46] J. Matheis, S. Hickel, Multi-component vapor-liquid equilibrium model for LES of high-pressure fuel injection and application to ECN Spray A, *International Journal of Multiphase Flow* 99 (2018) 294–311.
- 610 [47] P. Ma, H. Wu, T. Jaravel, L. Bravo, M. Ihme, Large-eddy simulations of transcritical injection and auto-ignition using diffuse-interface method and finite-rate chemistry, *Proceedings of the Combustion Institute* 37 (2019) 3303–3310.
- 615 [48] S. Yang, P. Yi, C. Habchi, Real-fluid injection modeling and LES simulation of the ECN Spray A injector using a fully compressible two-phase flow approach, *International Journal of Multiphase Flow* 122 (2020) 103145.
- [49] A. H. Lefebvre, V. G. McDonell, *Atomization and Sprays*, CRC Press, 2017. doi:10.1201/9781315120911.
- 620 [50] J. Brackbill, D. Kothe, C. Zemach, A continuum method for modeling surface tension, *Journal of Computational Physics* 100 (1992) 335–354.
- [51] G. Perigaud, R. Saurel, A compressible flow model with capillary effects, *Journal of Computational Physics* 209 (2005) 139–178.

- 625 [52] R. Saurel, C. Pantano, Diffuse-Interface Capturing Methods for Compressible Two-Phase Flows, *Annual Review of Fluid Mechanics* 50 (2018) 105–130.
- [53] L. Cheng, N. Barleon, O. Vermorel, B. Cuenot, A. Bourdon, AVIP: a low temperature plasma code, *arXiv e-print* 2201.01291 (2022).
- 630 [54] H. Lund, A Hierarchy of Relaxation Models for Two-Phase Flow, *SIAM Journal on Applied Mathematics* 72 (2012) 1713–1741.
- [55] S. Le Martelot, R. Saurel, O. Le Métayer, Steady one-dimensional nozzle flow solutions of liquid–gas mixtures, *Journal of Fluid Mechanics* 737 (2013) 146–175.
- 635 [56] S. Le Martelot, R. Saurel, B. Nkonga, Towards the direct numerical simulation of nucleate boiling flows, *International Journal of Multiphase Flow* 66 (2014) 62–78.
- [57] T. Poinso, D. Veynante, *Theoretical and Numerical Combustion*, 3rd ed., 2012.
- 640 [58] G. Soave, Equilibrium constants from a modified Redlich–Kwong equation of state, *Chemical Engineering Science* 27 (1972) 1197–1203.
- [59] D.-Y. Peng, D. B. Robinson, A New Two-Constant Equation of State, *Industrial & Engineering Chemistry Fundamentals* 15 (1976) 59–64.
- [60] O. Le Métayer, R. Saurel, The Noble–Abel Stiffened–Gas equation of state, 645 *Physics of Fluids* 28 (2016) 046102.
- [61] P. Boivin, M. A. Cannac, O. Le Métayer, A thermodynamic closure for the simulation of multiphase reactive flows, *International Journal of Thermal Sciences* 137 (2019) 640–649.
- 650 [62] J. Carmona, Modélisation des phénomènes diphasiques dans des injecteurs aéronautiques de type Airblast, Ph.D. thesis, Institut National Polytechnique de Toulouse, 2021.
- [63] T. J. Poinso, S. K. Lele, Boundary conditions for direct simulations of compressible viscous flows, *Journal of Computational Physics* 101 (1992) 104–129.
- 655 [64] K. W. Thompson, Time dependent boundary conditions for hyperbolic systems, *Journal of Computational Physics* 68 (1987) 1–24.
- [65] N. Okong'o, J. Bellan, Consistent Boundary Conditions for Multicomponent Real Gas Mixtures Based on Characteristic Waves, *Journal of Computational Physics* 176 (2002) 330–344.
- 660 [66] T. Schönfeld, M. Rudgyard, Steady and Unsteady Flow Simulations Using the Hybrid Flow Solver AVBP, *AIAA Journal* 37 (1999) 1378–1385.

- [67] L. Y. Gicquel, N. Gourdain, J.-F. Boussuge, H. Deniau, G. Staffelbach, P. Wolf, T. Poinsot, High performance parallel computing of flows in complex geometries, *Comptes Rendus Mécanique* 339 (2011) 104–124.
- 665 [68] W. Sutherland, LII. The viscosity of gases and molecular force, *Philosophical Magazine Series 5* 36 (1893) 507–531.
- [69] E. F. Toro, M. Spruce, W. Speares, Restoration of the contact surface in the HLL-Riemann solver, *Shock Waves* 4 (1994) 25–34.
- 670 [70] P. K. Sweby, High Resolution Schemes Using Flux Limiters for Hyperbolic Conservation Laws, *SIAM Journal on Numerical Analysis* 21 (1984) 995–1011.
- [71] N. Lamarque, Schémas numériques et conditions limites pour la simulation aux grandes échelles de la combustion diphasique dans les foyers d’hélicoptère, Ph.D. thesis, Institut National Polytechnique de Toulouse, 2007.
- 675 [72] L. Segui-Troth, Multi-physics coupled simulations of gas turbines, Ph.D. thesis, Institut National Polytechnique de Toulouse, 2017.
- [73] S. Mirjalili, C. B. Ivey, A. Mani, Comparison between the diffuse interface and volume of fluid methods for simulating two-phase flows, *International Journal of Multiphase Flow* 116 (2019) 221–238.
- 680 [74] P. J. Linstrom, W. G. Mallard, The NIST Chemistry WebBook: A Chemical Data Resource on the Internet, *Journal of Chemical & Engineering Data* 46 (2001) 1059–1063.
- [75] L. Rayleigh, On the Capillary Phenomena of Jets, *Proceedings of The Royal Society of London* 29 (1879) 71–97.
- 685 [76] D. Fyfe, O. E.S, M. Fritts, Surface tension and viscosity with lagrangian hydrodynamics on a triangular mesh, *Journal of Computational Physics* 76 (1988) 349–384.
- [77] G. Vaudor, T. Ménard, W. Aniszewski, M. Doring, A. Berlemont, A consistent mass and momentum flux computation method for two phase flows. Application to atomization process, *Computers & Fluids* 152 (2017) 204–216.
- 690 [78] O. Colin, M. Rudgyard, Development of High-Order Taylor–Galerkin Schemes for LES, *Journal of Computational Physics* 162 (2000) 338–371.
- [79] P. Marmottant, E. Villermaux, Fragmentation of stretched liquid ligaments, *Physics of Fluids* 16 (2004) 2732–2741.
- 695 [80] L. Raynal, Instabilité et entraînement à l’interface d’une couche de mélange liquide-gaz, Ph.D. thesis, Institut National Polytechnique de Grenoble, 1997.

- 700 [81] F. Ben Rayana, A. Cartellier, E. Hopfinger, et al., Assisted atomization of a liquid layer: investigation of the parameters affecting the mean drop size prediction, in: Proceedings of the International Conference on Liquid Atomization and Spray Systems (ICLASS), Kyoto, Japan, 2006, p. 8 pages.
- [82] F. Ben Rayana, Contribution à l'étude des instabilités interfaciales liquide-gaz en atomisation assistée et tailles de gouttes, Ph.D. thesis, Institut National Polytechnique de Grenoble, 2007.
- 705 [83] J.-P. Matas, S. Marty, A. Cartellier, Experimental and analytical study of the shear instability of a gas-liquid mixing layer, *Physics of Fluids* 23 (2011) 094112.
- [84] J. J. S. Jerome, S. Marty, J.-P. Matas, S. Zaleski, J. Hoepffner, Vortices catapult droplets in atomization, *Physics of Fluids* 25 (2013) 112109.
- [85] J.-P. Matas, S. Marty, M. Seydou Dem, A. Cartellier, Influence of Gas Turbulence on the Instability of an Air-Water Mixing Layer, *Physical Review Letters* 115 (2015).
- 715 [86] P. E. Dimotakis, Two-dimensional shear-layer entrainment, *AIAA Journal* 24 (1986) 1791–1796.
- [87] D. Fuster, A. Bagué, T. Boeck, L. Le Moyne, A. Leboissetier, S. Popinet, P. Ray, R. Scardovelli, S. Zaleski, Simulation of primary atomization with an octree adaptive mesh refinement and VOF method, *International Journal of Multiphase Flow* 35 (2009) 550–565.
- 720 [88] D. Fuster, J.-P. Matas, S. Marty, S. Popinet, J. Hoepffner, A. Cartellier, S. Zaleski, Instability regimes in the primary breakup region of planar coflowing sheets, *Journal of Fluid Mechanics* 736 (2013) 150–176.
- [89] G. Agbaglah, R. Chiodi, O. Desjardins, Numerical simulation of the initial destabilization of an air-blasted liquid layer, *Journal of Fluid Mechanics* 812 (2017) 1024–1038.
- 725 [90] O. Desjardins, J. McCaslin, M. Owkes, P. Brady, Direct Numerical and Large-Eddy Simulations of primary atomization in complex geometries, *Atomization and Sprays* 23 (2013) 1001–1048.
- 730 [91] C. Bozonnet, J.-P. Matas, G. Balarac, O. Desjardins, Stability of an air-water mixing layer: focus on the confinement effect, *Journal of Fluid Mechanics* 933 (2021).
- [92] R. Chiodi, O. Desjardins, A Numerical Parametric Study on the Air-Blast Atomization of a Planar Liquid Layer, in: 55<sup>th</sup> AIAA Aerospace Sciences Meeting, American Institute of Aeronautics and Astronautics, 2017, pp. 1–9. URL: <https://doi.org/10.2514/6.2017-1702>. doi:10.2514/6.2017-1702.
- 735



- [93] T. Otto, M. Rossi, T. Boeck, Viscous instability of a sheared liquid-gas interface: Dependence on fluid properties and basic velocity profile, *Physics of Fluids* 25 (2013) 032103.
- [94] P. Welch, The use of fast Fourier transform for the estimation of power spectra: A method based on time averaging over short, modified periodograms, *IEEE Transactions on Audio and Electroacoustics* 15 (1967) 70–73.
- [95] S. K. Godunov, I. Bohachevsky, Finite difference method for numerical computation of discontinuous solutions of the equations of fluid dynamics, *Matematičeskij sbornik* 47(89) (1959) 271–306.
- [96] P. D. Lax, B. Wendroff, Systems of conservation laws, *Communications on Pure and Applied Mathematics* 13 (1960) 217–237.
- [97] E. F. Toro, *Riemann Solvers and Numerical Methods for Fluid Dynamics*, Springer Berlin Heidelberg, 2009. doi:10.1007/b79761.
- [98] A. Chiapolino, R. Saurel, B. Nkonga, Sharpening diffuse interfaces with compressible fluids on unstructured meshes, *Journal of Computational Physics* 340 (2017) 389–417.
- [99] P. D. Lax, X.-D. Liu, Solution of Two-Dimensional Riemann Problems of Gas Dynamics by Positive Schemes, *SIAM Journal on Scientific Computing* 19 (1998) 319–340.
- [100] A. Kurganov, E. Tadmor, Solution of two-dimensional Riemann problems for gas dynamics without Riemann problem solvers, *Numerical Methods for Partial Differential Equations* 18 (2002) 584–608.

## Appendix A. Characteristic boundary conditions

Well applied boundary conditions are of major interest in compressible flows in order to avoid for example pressure drift and acoustic waves in the computational domain. A proper derivation of the coefficients from the Jacobian matrix is essential as is the speed of sound.

One can recall the one-dimensional 4-equation model

$$\frac{\partial \mathbf{U}}{\partial t} + \frac{\partial \mathbf{F}(\mathbf{U})}{\partial x} = 0, \quad (\text{A.1})$$

where  $\mathbf{U} = [\rho, \rho \mathbf{u}, \rho E, \rho Y_k]^t$  and  $\mathbf{F} = [\rho \mathbf{u}, \rho \mathbf{u} \otimes \mathbf{u} + P, (\rho E + P)\mathbf{u}, \rho Y_k \mathbf{u}]^t$ .

Jacobian matrix reads

$$A_x(\mathbf{U}) = \frac{\partial \mathbf{F}(\mathbf{U})}{\partial \mathbf{U}} = \begin{bmatrix} 0 & 1 & 0 & 0 & \cdots & 0 \\ -\mathbf{u}^2 & \mathbf{u}(2 - \Lambda) & \Lambda & -\Lambda(\Gamma_1 - e_c) & \cdots & -\Lambda(\Gamma_N - e_c) \\ -\mathbf{u}H & H - \Lambda\mathbf{u}^2 & \mathbf{u}(1 + \Lambda) & -\mathbf{u}\Lambda(\Gamma_1 - e_c) & \cdots & -\mathbf{u}\Lambda(\Gamma_N - e_c) \\ -\mathbf{u}Y_1 & Y_1 & 0 & \mathbf{u} & \cdots & 0 \\ \vdots & \vdots & \vdots & \vdots & \ddots & \vdots \\ -\mathbf{u}Y_N & Y_N & 0 & 0 & \cdots & \mathbf{u} \end{bmatrix}, \quad (\text{A.2})$$

$$\text{with } H = E + P/\rho, \Lambda = \left. \frac{\partial P}{\partial \rho e} \right|_{\rho Y_k} \text{ and } \Gamma = \left. \frac{\partial \rho e}{\partial \rho Y_k} \right|_{P, \rho Y_{i \neq k}}.$$

#### Appendix A.1. Jacobian terms

770 This section proposes the derivation of the  $\Gamma$  and  $\Lambda$  coefficient involved in the jacobian matrix (Eq. (A.2)).

From the mixture laws one can write

$$e = \sum_{k=1}^N Y_k e_k, \quad (\text{A.3})$$

$$v = \sum_{k=1}^N Y_k v_k. \quad (\text{A.4})$$

Derivatives of previous expressions read

$$de = \sum_{k=1}^N Y_k de_k + \sum_{k=1}^N e_k dY_k, \quad (\text{A.5})$$

$$dv = \sum_{k=1}^N Y_k dv_k + \sum_{k=1}^N v_k dY_k. \quad (\text{A.6})$$

Species energy and volume derivatives can be written as

$$\begin{aligned} de_k &= \left. \frac{\partial e_k}{\partial P} \right|_T dP + \left. \frac{\partial e_k}{\partial T} \right|_P dT, \\ &= \frac{P\beta - T\alpha}{\rho} dP + \left( \bar{C}_p - \frac{P\alpha}{\rho} \right) dT, \end{aligned} \quad (\text{A.7})$$

$$\begin{aligned} dv_k &= \left. \frac{\partial v_k}{\partial P} \right|_T dP + \left. \frac{\partial v_k}{\partial T} \right|_P dT, \\ &= -v\beta dP + v\alpha dT, \end{aligned} \quad (\text{A.8})$$

where  $\alpha$  and  $\beta$  are defined in appendix Appendix A.2.

So Eqs. (A.5) and (A.6) can be rewritten as

$$de = \sum_{k=1}^N Y_k \left( \frac{P\beta - T\alpha}{\rho} dP + \left( \bar{C}_p - \frac{P\alpha}{\rho} \right) dT \right) + \sum_{k=1}^N e_k dY_k, \quad (\text{A.9})$$

$$dv = \sum_{k=1}^N Y_k (-v\beta dP + v\alpha dT) + \sum_{k=1}^N v_k dY_k. \quad (\text{A.10})$$

With Eq. (A.10) one can write

$$dT = -\frac{1}{\rho\alpha} d\rho + \frac{\beta}{\alpha} dP - \frac{\rho}{\alpha} \sum_{k=1}^N v_k dY_k. \quad (\text{A.11})$$

So Eq. (A.5) becomes

$$\begin{aligned} de &= \frac{1}{\rho} \left( \frac{\rho\bar{C}_p\beta}{\alpha} - \alpha T \right) dP + \frac{1}{\rho^2} \left( P - \frac{\rho\bar{C}_p}{\alpha} \right) d\rho \\ &\quad - \frac{\rho\bar{C}_p}{\alpha} \sum_{k=1}^N v_k dY_k + \sum_{k=1}^N h_k dY_k. \end{aligned} \quad (\text{A.12})$$

775 Knowing that  $d(\rho e) = \rho de + e d\rho$ ,

$$d(\rho e) = \left( \frac{\rho\bar{C}_p\beta}{\alpha} - \alpha T \right) dP + \sum_{k=1}^N \left( h_k - \frac{\rho\bar{C}_p}{\alpha\rho_k} \right) d(\rho Y_k). \quad (\text{A.13})$$

Finally one can write

$$\Lambda = \left. \frac{\partial P}{\partial \rho e} \right|_{\rho Y_k} = \frac{1}{\frac{\rho\bar{C}_p\beta}{\alpha} - \alpha T}, \quad (\text{A.14})$$

$$\Gamma = \left. \frac{\partial \rho e}{\partial \rho Y_k} \right|_{P, Y_{i \neq k}} = h_k - \frac{\rho\bar{C}_p}{\alpha\rho_k}. \quad (\text{A.15})$$

### Appendix A.2. Isobaric dilatation and isotherm compressibility coefficients

The Isobaric dilatation  $\alpha$  and isothermal compressibility  $\beta$  coefficients respectively read

$$\alpha = \frac{1}{v} \left. \frac{\partial v}{\partial T} \right|_{P, \mathbf{Y}} = -\frac{1}{\rho} \left. \frac{\partial \rho}{\partial T} \right|_{P, \mathbf{Y}}, \quad (\text{A.16})$$

$$\beta = -\frac{1}{v} \left. \frac{\partial v}{\partial P} \right|_{T, \mathbf{Y}} = \frac{1}{\rho} \left. \frac{\partial \rho}{\partial P} \right|_{T, \mathbf{Y}}. \quad (\text{A.17})$$

In a multicomponent NASG framework the mass-specific volume reads

$$v(T, P, Y_k) = \sum_{k=1}^N Y_k \left( \frac{(\gamma_k - 1)C_{v,k}T}{P + P_{\infty,k}} + b_k \right), \quad (\text{A.18})$$

so that the mixture mass-specific volume derivative at constant composition reads

$$dv = \sum_{k=1}^N Y_k \left( \frac{(\gamma_k - 1)C_{v,k}(P + P_{\infty,k})dT - (\gamma_k - 1)C_{v,k}TdP}{(P + P_{\infty,k})^2} \right). \quad (\text{A.19})$$

780 The mass volume is related to density through

$$\rho = \frac{1}{v}, \quad \text{and} \quad d\rho = -\rho^2 dv. \quad (\text{A.20})$$

So the density derivative reads

$$d\rho = -\rho^2 \sum_{k=1}^N \left( \frac{(\gamma_k - 1)C_{v,k}(P + P_{\infty,k})(Y_k dT + T dY_k) - Y_k(\gamma_k - 1)C_{v,k}TdP}{(P + P_{\infty,k})^2} \right). \quad (\text{A.21})$$

Finally one can write

$$\alpha = \rho \sum_{k=1}^N Y_k \left( \frac{(\gamma_k - 1)C_{v,k}}{P + P_{\infty,k}} \right), \quad (\text{A.22})$$

$$\beta = \rho \sum_{k=1}^N Y_k \left( \frac{(\gamma_k - 1)C_{v,k}T}{(P + P_{\infty,k})^2} \right). \quad (\text{A.23})$$

### Appendix A.3. Speed of sound

The hyperbolic sound speed reads

$$c^2 = \left. \frac{\partial P}{\partial \rho} \right|_{s, \mathbf{Y}}, \quad (\text{A.24})$$

with composition  $\mathbf{Y} = [Y_1, \dots, Y_N]^t$ .

785 The differential of the mixture mass-specific volume at constant composition can be written as

$$\begin{aligned} dv &= \left. \frac{\partial v}{\partial T} \right|_{P, \mathbf{Y}} dT + \left. \frac{\partial v}{\partial P} \right|_{T, \mathbf{Y}} dP, \\ &= v\alpha dT - v\beta dP, \end{aligned} \quad (\text{A.25})$$

so that

$$dT = -\frac{1}{\rho\alpha} d\rho + \frac{\beta}{\alpha} dP. \quad (\text{A.26})$$

The mixture mass specific entropy reads

$$\begin{aligned} s(P, T, Y_k) &= \sum_{k=1}^N Y_k s_k(P, T), \\ &= \sum_{k=1}^N Y_k \left( C_{v,k} \ln \left( \frac{T^{\gamma_k}}{(P + P_{\infty,k})^{\gamma_k - 1}} \right) + s_k^0 \right), \end{aligned} \quad (\text{A.27})$$

where  $C_{v,k}$ ,  $s_k^0$ ,  $P_{\infty,k}$  are specific constants of the NASG thermodynamics framework. The mixture mass specific entropy differential at constant composition  
790 reads

$$\begin{aligned} ds &= \left. \frac{\partial s}{\partial T} \right|_{P,\mathbf{Y}} dT + \left. \frac{\partial s}{\partial P} \right|_{T,\mathbf{Y}} dP, \\ &= \frac{\bar{C}_p}{T} dT - \frac{\alpha}{\rho} dP. \end{aligned} \quad (\text{A.28})$$

Casting Eq. (A.26) into Eq. (A.28) yields

$$ds = -\frac{1}{\rho\alpha} \frac{\bar{C}_p}{T} d\rho + \left( -\frac{\alpha}{\rho} + \frac{\bar{C}_p}{T} \frac{\beta}{\alpha} \right) dP. \quad (\text{A.29})$$

Finally, the hyperbolic 4-equation system sound speed reads

$$c^2 = \frac{\bar{C}_p}{\rho\beta\bar{C}_p - \alpha^2 T}, \quad (\text{A.30})$$

with  $\bar{C}_p = \sum_{k=1}^N Y_k C_{p,k}$ .

## Appendix B. A Vertex-centered HLLC-MUSCL scheme

### 795 Appendix B.1. Scheme implementation in a Vertex-Centered framework

Godunov numerical schemes [95] are usually implemented using a cell-centered framework. Fluxes are estimated on cell faces and conservative variables stored at the cell centre. The AVBP solver features a cell-vertex architecture, which offers an efficient way of handling numerical schemes like Lax-Wendroff or Taylor-  
800 Galerkin schemes [78, 96]. The Godunov scheme implemented in this work relies therefore on a node-centered formalism.

It considers the integral form of the transport equations, written in the compact form as

$$\frac{\partial}{\partial t} \int_V \mathbf{U} dV + \oint_{\partial V} \mathbf{F} \cdot \mathbf{n} dS = 0. \quad (\text{B.1})$$

The integration is made on the nodal volume  $V_i$  associated to node  $i$ , illustrated  
805 by the grey area in Fig. B.11. Fluxes are computed at all nodal volume faces, determined from the intersection of  $V_i$  surface with all cells  $\tau$  containing the node  $i$ , and noted  $E(i)$

$$\frac{\partial}{\partial t} \mathbf{U}_i + \sum_{\tau \in E(i)} \sum_{f \in V_i \cap \tau} \int_f \mathbf{F} \cdot \mathbf{n} dS = 0. \quad (\text{B.2})$$

In Eq. (B.2), the first sum corresponds to a loop over all cells containing a given node, while the second sum corresponds to a loop over the faces of the nodal  
810 volume  $V_i$ .

Surfaces integrals are computed by projecting the flux into the local basis of the edge as it is less computationally expensive than splitting the flux in 3 components in a fixed basis dimension and solving 3 Riemann problems ([97], Ch. 16).

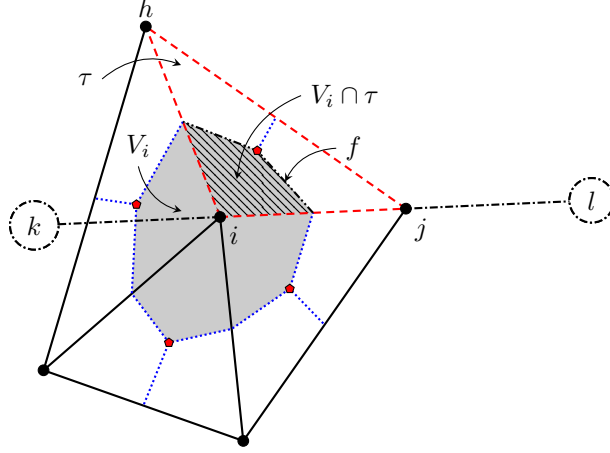


Figure B.11: Discretization at all the cell nodes. The grey area represents the nodal volume  $V_i$ . The hatched area is the intersection of a cell  $\tau$  containing node  $i$  with the nodal volume  $V_i$ . The edges of  $V_i$  ( $f$ ) are defined from the center of cell  $\tau$  and the middle of its edges with node  $i$  ( $j$  and  $h$ ). The virtual nodes  $k$  and  $l$  are used for the MUSCL procedure.

### 815 Appendix B.2. MUSCL reconstruction procedure

A HLLC Riemann solver [69] is considered in this work with a MUSCL reconstruction of variables to compute fluxes at edges. This procedure uses piecewise linear functions to ensure second order accuracy. Cell boundary values are computed as  $\mathbf{U}_i^L = \mathbf{U}_i^n - \Delta\mathbf{U}_i^n/2$  and  $\mathbf{U}_i^R = \mathbf{U}_i^n + \Delta\mathbf{U}_i^n/2$  respectively on the left and on the right sides of node  $i$  along a given direction. For stability  $\Delta\mathbf{U}_i^n$  is computed with the limited approach of Sweby [70]:

$$\Delta\mathbf{U}_i^n = \begin{cases} \begin{cases} \max\left[0, \min\left(\beta\Delta\mathbf{U}_{i-1/2}^n, \Delta\mathbf{U}_{i+1/2}^n\right), \right. \\ \left. \min\left(\Delta\mathbf{U}_{i-1/2}^n, \beta\Delta\mathbf{U}_{i+1/2}^n\right)\right], & \text{if } \Delta\mathbf{U}_{i+1/2}^n > 0, \\ \min\left[0, \max\left(\beta\Delta\mathbf{U}_{i-1/2}^n, \Delta\mathbf{U}_{i+1/2}^n\right), \right. \\ \left. \max\left(\Delta\mathbf{U}_{i-1/2}^n, \beta\Delta\mathbf{U}_{i+1/2}^n\right)\right], & \text{if } \Delta\mathbf{U}_{i+1/2}^n < 0, \end{cases} \end{cases} \quad (\text{B.3})$$

where  $\beta \in [1, 2]$  is a limiter parameter.

The  $\Delta\mathbf{U}_{i-1/2}^n$  and  $\Delta\mathbf{U}_{i+1/2}^n$  values correspond respectively to  $\Delta_{ki}$  and  $\Delta_{ij}$  for the node  $i$  and  $\Delta_{ij}$  and  $\Delta_{jl}$  for the node  $j$  as shown in Fig. B.11. In the case of irregular meshes in Fig. B.11 virtual nodes are retrieved (dash-dotted circles):  $k$  and  $l$  are respectively at a distance  $\mathbf{ij}$  of  $i$  and  $j$ .

### Appendix B.3. Hyperbolic solver validation

#### Appendix B.3.1. One dimensional shock-tube

The solver is first validated on a two-phase shock tube configuration without surface tension (Sys. (2)). The present study considers a shock tube that is 1 m long and comprised of two chambers, which are separated by an interface

Table B.5: SG thermodynamic coefficients for H<sub>2</sub>O (liquid) and Air species.

Coefficients	H <sub>2</sub> O (liquid)	Air
$C_{p,k}$ [J.kg <sup>-1</sup> .K <sup>-1</sup> ]	4400	1001
$C_{v,k}$ [J.kg <sup>-1</sup> .K <sup>-1</sup> ]	1000	715
$P_{\infty,k}$ [Pa]	$6 \times 10^8$	0
$q_k$ [J.kg <sup>-1</sup> ]	0	0
$b_k$ [m <sup>3</sup> .kg <sup>-1</sup> ]	0	0

located at  $x = 0.7$  m. The left side is filled with liquid water at  $P = 1$  GPa and  $\rho = 1000$  kg.m<sup>-3</sup>. The right side is composed of air at  $P = 1 \times 10^5$  Pa and  $\rho = 10$  kg.m<sup>-3</sup>. The left chamber contains a small amount of air  $Y_{\text{air}} = 10^{-8}$ .  
 835 The right chamber has a reversed composition. Thermodynamic properties are displayed in Tab. B.5. The covolume for species H<sub>2</sub>O is zero to retrieve the Stiffened-Gas (SG) EoS. The 1D computational domain is divided into 2000 uniform elements.

Results are shown in Fig. B.12, where plots of pressure, density, velocity and  
 840 liquid volume fraction are depicted at  $t = 220$   $\mu$ s, and compared to the exact solution. Agreement is seen to be excellent. Consistently with the literature [34, 98], no overshoot is obtained, and Hugoniot relationships are satisfied.

### Appendix B.3.2. Two dimensional Riemann test case

Two dimensional Riemann ideal gas test-cases are then considered. The  
 845 geometry is a  $[-0.5, -0.5] \times [0.5, 0.5]$  meter square with a  $600 \times 600$  regular grid. Specific calorific capacities ratio is constant and equal to  $\gamma = 1.4$ . The initial condition consists in four quadrants with different initial conditions [99]:

$$(\rho_0, \mathbf{u}_0, \mathbf{v}_0, P_0) = \begin{cases} (3.0, 0.75, 0.5, 1.0) & x \leq 0, y \geq 0, \\ (1.0, -0.75, 0.5, 1.0) & x \leq 0, y \leq 0, \\ (1.0, 0.75, -0.5, 1.0) & x \geq 0, y \geq 0, \\ (2.0, -0.75, -0.5, 1.0) & x \geq 0, y \leq 0. \end{cases} \quad (\text{B.4})$$

Results obtained at CFL = 0.7 and for a  $\beta$ -Sweeby parameter equal to 1.5  
 850 are shown in Fig. B.13a. It evidences the fact that the numerical solver is able to capture and transport stiff gradients with robustness and accuracy.

Other test-cases from Lax and Liu [99], Kurganov and Tadmor [100] are conducted, introducing rarefaction and shock waves in addition to the contact discontinuity. The initial states are defined thanks to Eqs. (B.5) and (B.6), and results are presented in Figs. B.13b and B.13c. Results are again very satisfying.

$$(\rho_0, \mathbf{u}_0, \mathbf{v}_0, P_0) = \begin{cases} (3.0, -0.6259, 0.1, 1.0) & x \leq 0, y \geq 0, \\ (0.8, 0.1, 0.1, 1.0) & x \leq 0, y \leq 0, \\ (0.5197, 0.1, 0.1, 0.4) & x \geq 0, y \geq 0, \\ (1.0, 0.1, -0.6259, 1.0) & x \geq 0, y \leq 0. \end{cases} \quad (\text{B.5})$$

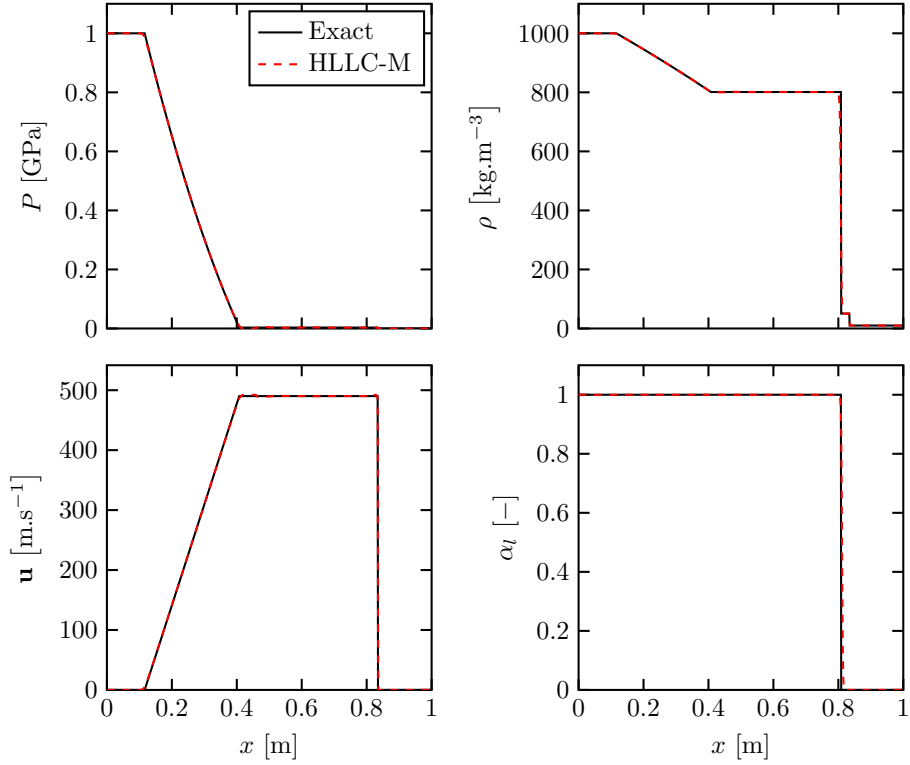
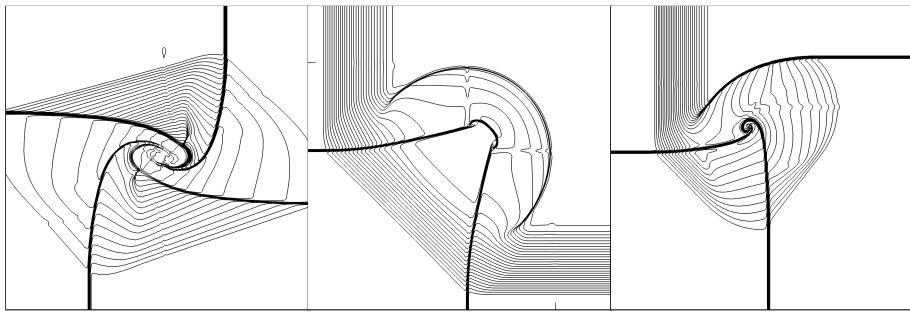


Figure B.12: Liquid-gas shock tube results at  $t = 220 \mu\text{s}$  at  $\text{CFL} = 0.5$ .



(a) Configuration of Eq. (B.4). (b) Configuration of Eq. (B.5). (c) Configuration of Eq. (B.6).

Figure B.13: Density isocontours (60 lines) on a  $600 \times 600$  grid at (a)  $t = 0.3 \text{ s}$ , (b)  $t = 0.25 \text{ s}$ , (c)  $t = 0.2 \text{ s}$ . The numerical scheme is HLLC-M RK3 with  $\text{CFL} = 0.7$ . The wave configurations are the following: (a) 4 contact discontinuities, (b) 2 contact discontinuities, 2 rarefaction waves, (c) 1 shock wave, 1 rarefaction wave, 2 contact discontinuities.



$$(\rho_0, \mathbf{u}_0, \mathbf{v}_0, P_0) = \begin{cases} (1.0, -0.6179, 0.1, 1.0) & x \leq 0, y \geq 0, \\ (0.8, 0.1, 0.1, 0.4) & x \leq 0, y \leq 0, \\ (0.5313, 0.1, 0.1, 1.0) & x \geq 0, y \geq 0, \\ (1.0, 0.1, 0.8276, 1.0) & x \geq 0, y \leq 0. \end{cases} \quad (\text{B.6})$$

### Appendix B.3.3. Order of accuracy

The order of accuracy of the scheme is next assessed thanks to the convection of an isentropic Gaussian vortex, defined with the following functions

$$v'_r = 0, \quad v'_\theta = \frac{\Gamma r}{R_c^2} \exp\left(-\frac{r^2}{2R_c^2}\right), \quad (\text{B.7})$$

while the temperature writes

$$T' = -\frac{\Gamma^2}{2C_p R_c^2} \exp\left(-\frac{r^2}{R_c^2}\right), \quad (\text{B.8})$$

860 where  $r = \sqrt{x^2 + y^2}$ . The pressure finally results from

$$P = P_\infty \left(\frac{T}{T_\infty}\right)^{\frac{\gamma}{\gamma-1}}. \quad (\text{B.9})$$

Tests are conducted on a  $[0, 0] \times [0.1, 0.1]$  meter square domain, filled with air, with periodic boundary conditions. Pressure and temperature are set to 101 325 Pa and 300 K. The mean velocity is  $100 \text{ m}\cdot\text{s}^{-1}$  while the vortex is characterized by a  $R_c = 1 \text{ cm}$  radius and a  $\Gamma = 1 \text{ m}^2\cdot\text{s}^{-1}$  strength.

865 The different profiles of density after one convective time depending on the limiter parameter  $\beta$  are shown in Fig. B.14. The MUSCL reconstruction allows to recover a correct solution without excessive diffusion.

A mesh convergence study is conducted to assess the spatial order accuracy of the scheme from  $32 \times 32$  to  $2048 \times 2048$  cells grids.  $\mathcal{L}^2$ -error for the density, 870 where the  $\mathcal{L}^2$ -error is defined as

$$\mathcal{L}^2(\varepsilon_\rho) = \sqrt{\frac{\sum_i V_i (\tilde{\rho}_i - \rho_i)^2}{\sum_i V_i}}, \quad (\text{B.10})$$

with  $\tilde{\rho}$  the exact solution and  $V_i$  the node volumes, is shown in Fig. B.15 at CFL = 0.7 for HLLC-MUSCL. A second-order accuracy is recovered, with the slope limiter parameter  $\beta$  having an influence only for coarse meshes.

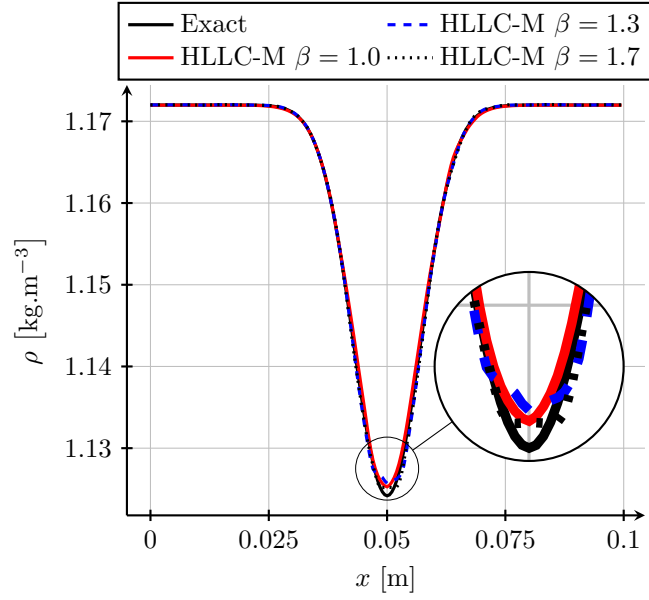


Figure B.14: Comparison of the schemes after one convective time with  $256 \times 256$  resolution.

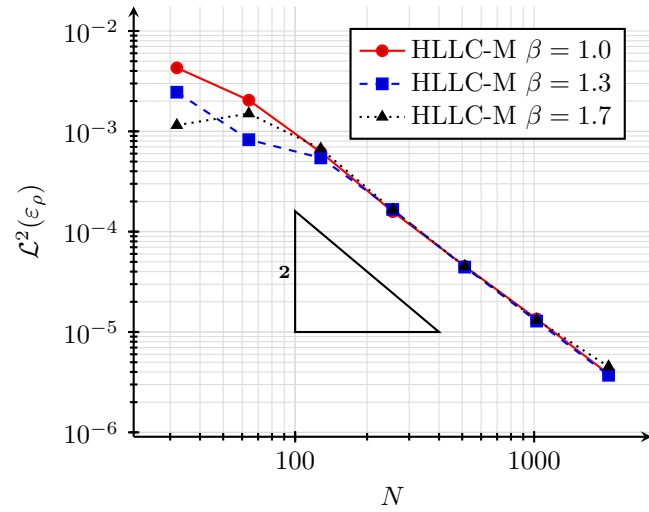


Figure B.15: Order of the schemes on the vortex test case after one convective time.